Lauri Kangas

White light interferometer for vibration analysis of low-frequency micromechanical resonators

School of Science

Thesis submitted for examination for the degree of Master of Science in Technology.

Espoo 06.03.2014

Thesis supervisor:

Prof. Matti Kaivola

Thesis instructor:

M.Sc. Kimmo Kokkonen

Aalto University
School of Science

AALTO UNIVERSITY
SCHOOL OF SCIENCE

ABSTRACT OF THE
MASTER'S THESIS

Author: Lauri Kangas

Title: White light interferometer for vibration analysis of low-frequency micromechanical resonators

Date: 06.03.2014 Language: English Number of pages: 6+66

School of Science

Department of Applied Physics

Professorship: Optics Code: Tfy-125

Supervisor: Prof. Matti Kaivola

Instructor: M.Sc. Kimmo Kokkonen

Micromechanical (MEMS) resonators are currently the subject of intensive research for applications in timing and frequency control. Due to their small size, low power consumption and compatibility with integrated circuits, they are being considered as alternatives for quartz oscillators.

Relying only on numerical modeling and electrical measurements has proven insufficient for understanding the behavior and validating designs of vibrating structures. Instead, direct optical measurements are needed for accurate dynamical characterization of vibration in the devices.

During the last decade, white light interferometry (WLI) has become an established method for making three-dimensional profile measurements of various surfaces in the microscale. This form of interferometry with low coherence light sources has the advantage of unambiguous surface height determination over interferometric applications using lasers or other monochromatic light sources. A vertical resolution below one nanometer can be achieved with suitable hardware and post processing techniques.

With synchronized stroboscopic illumination, a periodically vibrating object can effectively be "frozen" in place. This allows the use of stationary three-dimensional probing techniques to be used on vibrating samples. Using a CCD imaging sensor enables simultaneous spatial measurements over a wide area of interest. Therefore, stroboscopic imaging white light interferometry is an interesting alternative for vibration measurements of MEMS resonators.

In this thesis, a stroboscopic white light interferometer with a frequency range up to a few megahertz and a minimum detectable amplitude limit of one nanometer is designed, implemented and evaluated.

Keywords: white light interferometry, stroboscopic illumination, MEMS, resonator, vibration detection

AALTO-YLIOPISTO
PERUSTIETEIDEN KORKEAKOULU

DIPLOMITYÖN
TIIVISTELMÄ

Tekijä: Lauri Kangas

Työn nimi: Valkoisen valon interferometri matalan taajuuden mikromekaanisten resonaattoreiden värähtelyanalyysiin

Päivämäärä: 06.03.2014 Kieli: englanti Sivumäärä: 6+66

Perustieteiden korkeakoulu

Teknillisen fysiikan laitos

Professuuri: Optiikka Koodi: Tfy-125

Valvoja: prof. Matti Kaivola

Ohjaaja: DI Kimmo Kokkonen

Mikromekaanisia (MEMS) resonaattoreita pidetään hyvien ominaisuuksiensa, kuten pienen koon, alhaisen tehonkulutuksen ja integroitavuutensa ansiosta otollisina kvartsioskillaattoreiden korvaajina mm. langattoman tiedonsiirron ajastus- ja taajuussovelluksissa.

MEMS-resonaattoreiden viimeaikaisen nopean kehityksen yhteydessä matemaattisiin malleihin ja sähköisiin mittauksiin nojaaminen on osoittautunut riittämättömäksi MEMS-laitteiden toimintaa ja suorituskykyä tarkastellessa. MEMS-laitteiden värähtelyjen täsmällistä tutkimista varten tarvitaan suoria optisia mittauksia.

Viime vuosikymmenen aikana valkoisen valon interferometria on vakiintunut tehokkaaksi työkaluksi mikroskaalan pintojen kolmiulotteiseen mittaamiseen. Verrattuna perinteiseen monokromaattisen valon interferenssiin, valkoisen valon interferometrian etu on mahdollisuus mitata pinnan korkeus yksikäsitteisesti. Sopivalla laitteistolla ja tarkoilla signaalinkäsittelyalgoritmeilla voidaan saavuttaa alle nanometrin pystysuuntainen mittaustarkkuus.

Jaksollisesti värähtelevä liike voidaan näennäisesti pysäyttää käyttämällä pulssitettua valaistusta. Tämän ansiosta liikkumattomien kohteiden kolmiulotteiseen mittaamiseen tarkoitettuja keinoja voidaan soveltaa värähteleviin näytteisiin. Lisäksi CCD-kuvakennon käyttäminen mahdollistaa mittaamisen suurelta alueelta kerrallaan. Siksi pulssitettu, kuvantava valkoisen valon interferometria on mielenkiintoinen työkalu MEMS-resonaattoreiden värähtelyanalyysiin.

Tässä diplomityössä on suunniteltu ja toteutettu valkoisen valon interferometrinen mittauslaitteisto, joka mahdollistaa nanometriluokan värähtelyjen mittaamisen muutaman megahertsin taajuusalueelle asti.

Avainsanat: valkoisen valon interferometri, pulssitettu valaistus, MEMS, resonaattori, värähtelymittaus

Acknowledgements

This thesis was written in the Optics and Photonics research group in the Department of Applied Physics of Aalto University. I'm most grateful for the opportunity of getting five years of work experience with research very closely matching my interest in optics and imaging. I wish to thank Prof. Matti Kaivola for supervising the thesis and in particular my instructor Kimmo Kokkonen for valuable advice throughout the years.

Further thanks go to Lauri Lipiäinen, Igor Shavrin and Steffen Novotny for cooperation, Hannu Määttänen of Teknofokus for providing hardware and optics expertise at the early stage of the project, everyone in Pollux, PIK, `#sirius` and `!sauerkraut` for making the spare time worthwile, and my family for their support.

Espoo, 06.03.2014

Lauri Kare Jaakko Kangas

Contents

Chapter 1

Introduction

The transformation of electrical signals into minute mechanical vibration and vice versa can be utilized for designing a multitude of electronics components, used in various sensing applications or as resonators and filters needed in wireless communication. During the research and development of these electroacoustic devices, characterizing them via electrical measurements alone is found to be insufficient. [1]

Optical probing techniques have proven to be indispensable tools in direct mapping of vibration fields in the devices. In scanning laser interferometry, interference between laser beams is used for measuring sample surface vibration at a single point, which is then translated across the sample to acquire a vibration map. Scanning laser interferometry [2] produces measurements with unsurpassed quality of devices featuring sub-nanometer amplitude vibration at high frequencies in the megahertz and gigahertz range.

Micromechanical (MEMS) resonators, with their many beneficial features such as compact size, low power consumption and integrability to silicon circuits, are currently the subject of intensive research for applications in timing and frequency control. [3] Typically these devices operate in the frequency range of (sub)kilohertz to a few megahertz and feature vibration amplitudes of up to a micrometer. In recent years, those qualities, together with advances in camera and computer technology, have sparked the interest of using stroboscopic illumination and interferometric microscopy for mapping vibration across millions of imaging pixels simultaneously.

In this master's thesis, an interferometric imaging system for measurements of surface vibration is designed, implemented and characterized. The system utilizes scanning white light interferometry methods to obtain three-dimensional surface profiles of stationary targets. Stroboscopic illumination with short, synchronized light pulses is used for apparently halting the vibration in place and enabling the acquisition of stationary surface profiles during different phases of vibration.

Chapter 2

MEMS devices

MEMS (microelectromechanical systems) refers to a range of miniature electrical devices that utilize mechanical motion at the microscale. Typical sizes of MEMS devices are well below one millimeter, with structures as small as one micrometer. MEMS are, in general, small machines that are constructed by making use of semiconductor device fabrication techniques, familiar from manufacturing integrated electronic circuits.

Since the arrival of the basic processes of etching silicon in the 1960s [4], numerous and diverse applications of transducing electrical signals to minute mechanical motion and vice versa have been proposed, realized and capitalized. Common examples of mature designs for sensing physical quantities are pressure sensors based on a moving membrane [5] and accelerometers with cantilever beams [6].

Single crystal silicon has excellent electrical and mechanical properties [7], and is the most common material used in making MEMS components. Using silicon is also very economical because of the low cost of producing substrates and vast infrastructure available at the integrated electronic circuit industry. Other substrate materials currently researched and applied in MEMS fabrication include semiconductors like gallium arsenide, ceramics such as silicon carbide, as well as metals, glass and some polymers. [1]

2.1 MEMS resonators

Instead of MEMS designs that simply utilize deflecting elements which alter some electrical properties of the device, making use of mechanical resonances in the structure opens up a multitude of new applications. Creating gyroscopes [8] and other sensors [9] is possible by, e.g., monitoring the effect of angular acceleration on the resonator characteristics like resonant frequency, phase and magnitude.

During recent years, advancements in the fabrication methods of MEMS have opened the possibility of using MEMS resonators in radio frequency (RF) electronics. Using

MEMS in wireless communication is especially interesting due to the high integrability potential.

Modern mobile phones and numerous other wireless applications like Bluetooth devices rely on quartz crystals as reference oscillators. Piezoelectric quartz crystals require no bias voltage and are insensitive to changes in temperature. However, despite the miniaturization efforts, quartz crystals are still discrete bulky components on the circuit board. Unlike quartz, MEMS resonators can be miniaturized and matched to the form factor that is needed for modern hand held wireless devices. Silicon resonators can even be integrated together with their driving circuitry, which offers a single package for frequency reference and timing applications, saving board space. Replacing quartz oscillators could bring down the cost, power consumption and physical size of wireless computing.

In addition to reference oscillators, many other components in the radio architectures of modern communication devices such as switches, filters, impedance tuners and phase shifters can be realized with MEMS technology. [3] Instead of developing MEMS based replacements for individual components in traditional radio architectures, a full redesign may be necessary and prove to be suitable for low-power radios

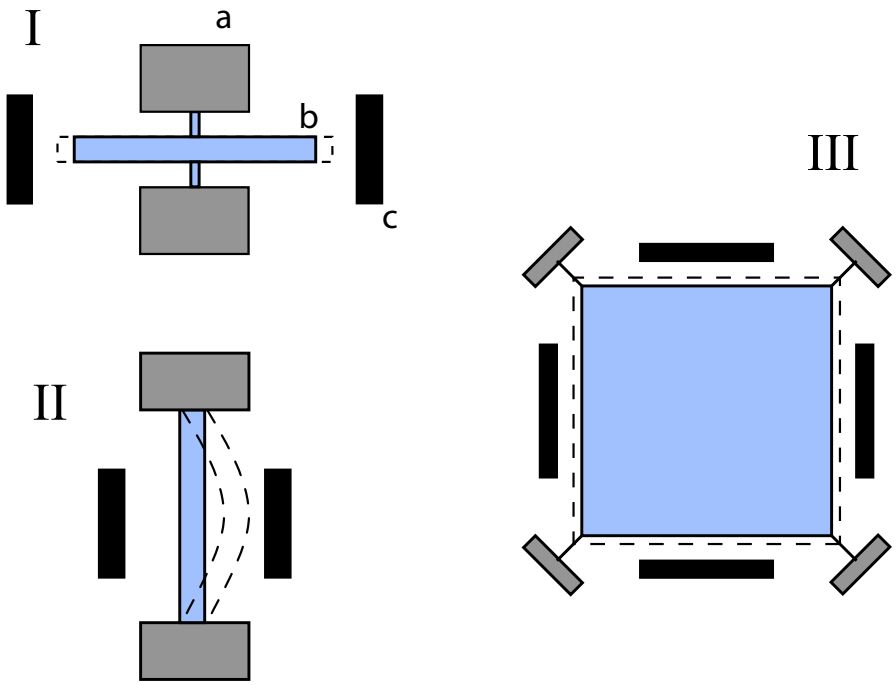

Figure 2.1. Typical MEMS resonator designs. The resonators feature (a) stationary anchoring locations, (b) vibrating silicon structures and (c) capacitive electrodes for driving the resonator with an electrical signal and sensing the response. The gap between the vibrating plate and the electrode is typically ca. 1 µm or less. **I)** A longitudinally vibrating beam, anchored from its center (bulk acoustic mode), **II)** a transversely vibrating beam anchored from its ends (flexural mode) and **III)** a corner-anchored square plate resonator vibrating in two dimensions.

in, e.g., wireless sensing applications. Many of the different operations in the radio circuit might be possible to implement as a single electromechanical device, when part of the signal processing is done in the mechanical domain. [10] These kind of designs will truly emphasize the devices as *systems* as the acronym MEMS suggests.

Even while the majority of MEMS resonators are CMOS-compatible and could be co-fabricated with electronic circuitry [11], it typically might not be advantageous for single devices. Compared to the micrometer scale patterns used in fabricating MEMS devices, the characteristic scale of integrated electronics is measured in tens of nanometers. Therefore, due to the differences in processing details, producing MEMS devices in a conventional CMOS factory might be too expensive. A promising workaround to combine these two worlds is processing a silicon-germanium (SiGe) based MEMS system on top of a CMOS electronic circuit. [12] This method allows a monolithic yet modular integration.

Typical MEMS resonator designs are illustrated in figure 2.1. The single beam resonator, with both ends either moving freely or being clamped, is a widely demonstrated geometry and is utilized in various vibrational modes. [13] [14] A square plate resonator geometry was recently used in the first MEMS resonator to meet the GSM specification for acceptable noise levels. [15]

2.2 Measurements of MEMS vibration

Various models for predicting the behavior of MEMS resonators exist, but these are presently not fully matured. [1] There are various microacoustic phenomena that the models have challenges explaining. These include spurious resonances (parasitic vibration modes) and unexpected losses in electrical response. Energy losses related to vibrating structure anchoring, fabrication defects and damping caused by ambient gas pressure are also left unaccounted for. [16]

As part of MEMS research, means of characterizing the actual vibration fields in a resonator are needed. A number of methods have been devised for directly measuring these vibrations in order to validate the design, operation and performance of the devices. Optical probing has proven to be an indispensable tool in MEMS development as a non-contact method of mapping surface vibration. The provided

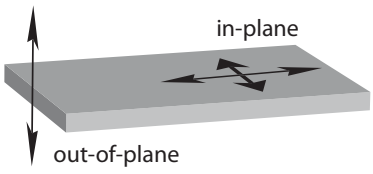

Figure 2.2. The three dimensional motion of a vibrating surface is divided into in-plane and out-of-plane components. In the orientation of this figure, the optical probing direction is from above.

physical information about the acoustic field in the resonator could not be obtained via measuring the electrical response.

The choice of optical probing method depends on the geometry of the motion. Surface vibration in MEMS resonators can happen both along the surface direction (in-plane) and perpendicular to it (out-of-plane), as illustrated in figure 2.2. The operation principles of optical measurement systems differ for the two kinds of vibration, and many alternative approaches have been demonstrated. [17]

With laser interferometry, the amplitude and phase of mechanical out-of-plane vibration in a resonator can be measured at a single spatial point using a tightly focused laser spot. Single-pixel measurements can be used, e.g., to obtain estimates of the quality factor of the resonance mode. [18] By translating the spot along the surface, a two-dimensional vibration field can be mapped to explore the vibration mode shapes. This *scanning laser interferometry* has been successfully employed in mapping the surface vibration of surface acoustic wave (SAW) and bulk acoustic wave (BAW) based ultrasonic devices with high frequencies in the gigahertz range and with out-of-plane vibration amplitudes as low as a few picometers. [1]

Scanning laser interferometry is also suitable for researching MEMS, where the devices typically have lower resonance frequencies and larger vibration amplitudes, when compared to those of typical SAW or BAW devices. An example of an interferometric MEMS vibration measurement is shown in figure 2.3. The amplitude of the out-of-plane vibration in a square plate MEMS resonator is measured with a setup described in more detail in section 3.1, page 11.

The resonator [15] is operating in the two-dimensional Lamé vibration mode in which two opposite sides of the square plate expand while the adjacent sides contract. The resonance is around 12 MHz. The plate expands and contracts laterally, in the plane of the surface.

Because of the positive Poisson's ratio ν of silicon [7] [19], the laterally deforming plate also changes its thickness. In the Lamé resonance, the in-plane vibration excites a complex out-of-plane vibration mode with multiple lobes as seen in figure 2.3b. This excitation makes it possible to use out-of-plane probing techniques on the frequency-dependent behavior of in-plane device.

A scanning laser interferometer can, in some situations, also be used for measurements of in-plane vibration. This novel technique [20] utilizes a modified Michelson interferometer, which does not record interference, but detects the intensity modulation of a single laser beam reflected from the sample. When the laser spot is on the edge of a laterally vibrating structure, the intensity of light reflecting back from the surface will oscillate. This enables the detection of very small (down to 20 pm) in-plane vibration amplitudes. The effect is observed at all edges and other reflectivity gradients on the sample surface. During fabrication, it is also possible to deposit metal dots or other features on the surface as optical targets.

Because of its sensitivity for detecting very low amplitudes, scanning laser interfer-

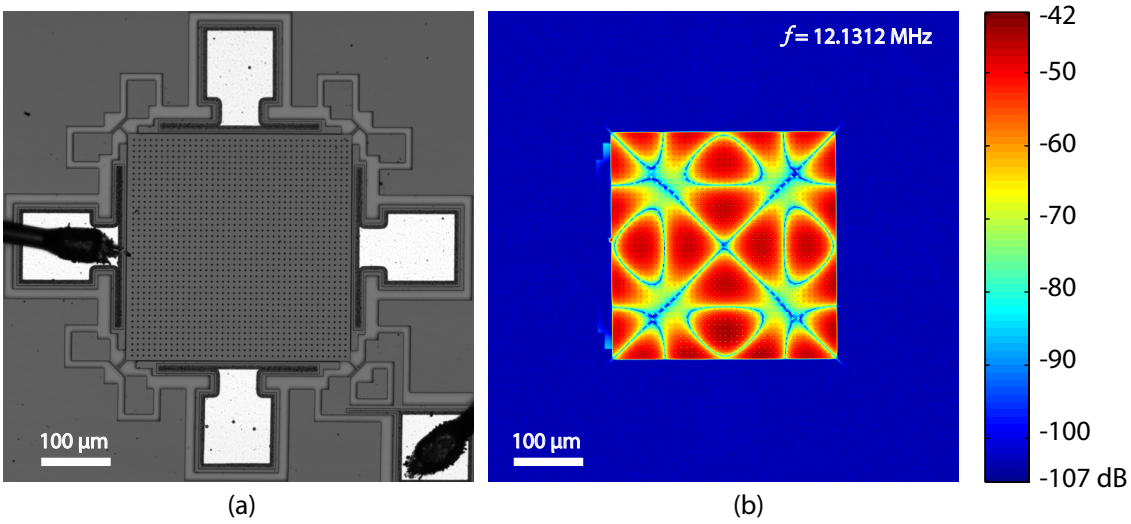

Figure 2.3. Example of a scanning laser interferometer measurement of out-of-plane vibration in a MEMS resonator. The sample is a square plate resonator operating at the frequency of its Lamé vibrational mode. [15] [19] **(a)** A map of reflected light power acquired during scanning the sample surface, equivalent to a microscope image of the sample. **(b)** The relative amplitude of vibration across the surface. The complex amplitude pattern represents the small out-of-plane component of the Lamé vibration mode, in which the motion is mainly taking place in the direction of the surface.

ometry is an unsurpassed tool in SAW and BAW device research. The sensitivity is a consequence of using the entire light power of the laser source in the measurement of a single point, recording the intensity with a high performance photo detector, and analyzing the oscillating signal with a spectrum analyzer. Disadvantages include high equipment costs and the need for scanning for measuring a large area.

Typical vibration amplitudes in low frequency MEMS devices are considerably larger than those of SAW or BAW devices. Measurements of larger amplitudes have less demand for sensitivity and allow building measurement setups based on lower cost detectors like cameras with CCD sensors.

Single photo detectors readily outperform the individual pixels in even the highest quality camera sensors, which experience higher noise and lower dynamic range compared to photo detectors. Camera pixels also record the cumulative amount of photons that hit the element during the exposure and are generally not well suited for making high speed measurements of intensity.

The advantage of using an image sensor, on the other hand, is its ability to separate spatial differences in the intensity of light. This allows a parallel measurement of up to millions of individual spatial pixels simultaneously, spanning the entire area of interest at once.

The acquisition of static microscope images of samples enable the detection of vibration on the surface. Microscopic imaging methods to detect in-plane vibration

include using a high speed video camera [21] or, assuming periodic vibration, using synchronized stroboscopic illumination. Advanced image processing methods allow sub-pixel detection of vibration, which allows a detection limit down in the nanometer scale. [22]

The measurement can be extended to the out-of-plane dimension by using interference microscopy, where light fields from the sample and a reference mirror interfere throughout the whole imaging plane. White light interferometry, described in detail in section 3.2, is an established technique in microscopic measurements of static topographies, i.e., three-dimensional measurements of the sample surface. Stroboscopic illumination can, again, be used to extend three-dimensional microscopic imaging for the detection of out-of-plane vibration of the measured surface. [23]

Chapter 3

Optical interference

Interference is evidence of the wave nature of light. By the 19th century, interferometry was known to be a good tool for accurate measurements but only had a few notable applications due to the limited coherence of the light sources then available. [24] One of the best known examples would be the Michelson-Morley experiment, which provided the first strong evidence against the theory of a luminiferous ether and in favor of special relativity. [25] After the invention of lasers in the 1960s, the greater coherence of the new light sources, as opposed to those used in the 19th century, allowed for a vast number of scientific and engineering applications based on interference of light.

Among those, the phenomenon is especially suitable for the measurement of small deflections of reflecting surfaces. Many interferometric detection systems are based on the variations of optical phase in the light wave when it is reflected from surfaces at varying distances. Because of the very high optical frequency of visible light (around 10^{14} Hz), the phase can not be directly observed with currently available detectors. Using interference, variation in phase can be transformed into variation in intensity, measurable in many different ways.

3.1 Two-beam interference

The geometry used in the Michelson-Morley experiment, the Michelson interferometer, is probably the most popular geometry used for optical interferometry today. [26] In a Michelson interferometer, illustrated in figure 3.1, a light beam is divided in two with a partially reflective plate or a beam splitter cube. The two light beams are reflected back by two planar surfaces and combined again with the same beam splitter. The superimposed beams interfere alters the intensity of the beam depending on the difference in the length of the optical path traveled by the divided beams.

For simplicity, consider the light beams as one-dimensional monochromatic waves with the same polarization, traveling along the optical axis z. The electrical fields

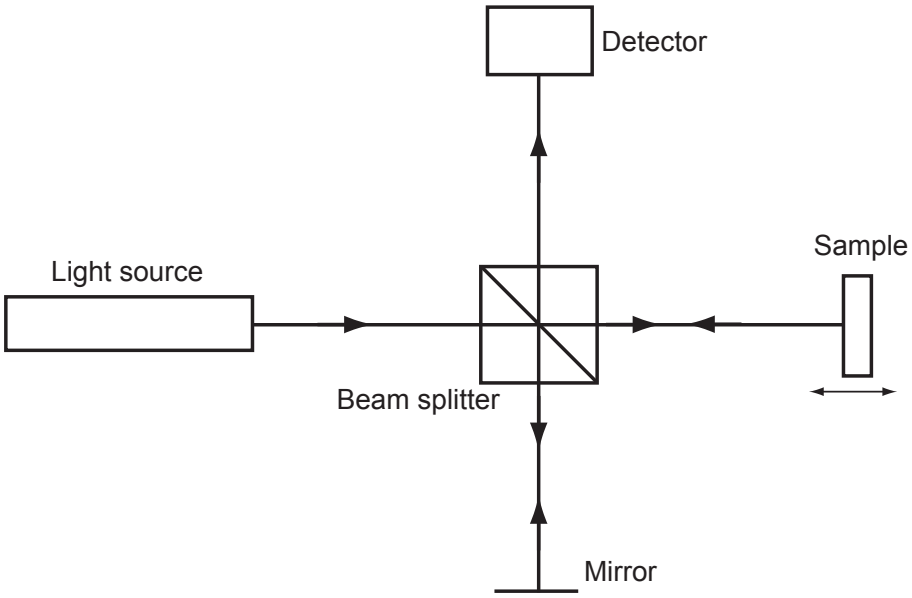

Figure 3.1. Basic layout of the Michelson interferometer. A light beam is divided with a semi-transparent mirror or a beam splitter cube. The light is reflect back of a sample and a reference mirror. The combined light beams interfere at the detector. The detected intensity will vary depending on small changes in the path lengths.

of these waves, as a function of z and time t, are

$$\begin{aligned} U_1(z,t) &= E_1 e^{i[\theta_1(z)-\omega t]} \\ U_2(z,t) &= E_2 e^{i[\theta_2(z)-\omega t]}, \end{aligned} \tag{3.1}$$

where E_i is the amplitude, θ_i the phase, and ω the angular frequency of the oscillating electrical field. The superimposed electrical field of the two waves is

$$U(z,t) = U_1(z,t) + U_2(z,t). \tag{3.2}$$

The intensities of a wave is found by $I_i(z) = |U_i|^2$. Calculating the inner product clears out the time-dependent imaginary part. Thus, the intensity of the superimposed beam will be

$$\begin{aligned} I &= |U|^2 \\ &= |U_1 + U_2|^2 \\ &= |U_1|^2 + |U_2|^2 + U_1^* U_2 + U_1 U_2^*. \end{aligned} \tag{3.3}$$

Now substituting waves (3.1) to equation (3.3) and denoting $\theta = \theta_2 - \theta_1$, we get

$$I = I_1 + I_2 + 2\sqrt{I_1 I_2}\cos(\theta). \tag{3.4}$$

This is called the interference equation and it shows that in addition to the incident intensities I_1 and I_2, the resulting intensity depends on the relative phase difference

θ of the two waves. What this means is that the intensity is not only a sum of the incident intensities, but also has an interference term depending on θ. The cosine term can be positive or negative which account for constructive or destructive interference, respectively.

Constructive interference occurs when $\theta = 0$, and

$$I_{max} = I_1 + I_2 + 2\sqrt{I_1 I_2}. \tag{3.5}$$

Similarly destructive interference occurs when $\theta = \pi$ and

$$I_{min} = I_1 + I_2 - 2\sqrt{I_1 I_2}. \tag{3.6}$$

θ varies when either mirror is translated axially. θ is related to the optical path difference OPD such that

$$\theta = OPD \cdot \frac{2\pi n}{\lambda}, \tag{3.7}$$

where n is the refractive index of the medium. In air, $n \approx 1$ and OPD equals the physical path length difference of the interferometer arms. It is worth noting that in a Michelson interferometer, displacing one of the mirrors by d makes the optical path difference change by $2d$ since the light will travel the same path twice, before and after reflecting from the mirror.

Due to changing θ, the detected intensity oscillates between I_{min} and I_{max}, forming an interference pattern. This spatial pattern is referred to as interference fringes. The visibility V of the interference fringes is then defined [26] by the relation

$$V = \frac{I_{max} - I_{min}}{I_{max} + I_{min}}, \tag{3.8}$$

where $0 \leq V \leq 1$. Substituting (3.5) and (3.6),

$$V = \frac{2\sqrt{I_1 I_2}}{I_1 + I_2}. \tag{3.9}$$

The visibility V quantifies the contrast of interference, such that $V = 1$ denotes best possible interference with bright constructive fringes and totally dark destructive fringes. $V = 0$ means no detectable interference at all. Further simplified, denoting $r = I_2/I_1$ ($I_2 < I_1$) gives $V = \sqrt{r}$. The intensity in equation (3.4) can now be written as

$$I(\theta) = I_{DC}(1 + V\cos(\theta)), \tag{3.10}$$

where I_{DC} is the sum of the two incident intensities with no interference.

As V only depends on the ratio of incident intensities, a special case with $I_1 = I_2 = I_0$ gives $V = 1$ and makes (3.4) vary between $0 \leq I \leq 4I_0$, depending on just the phase difference θ, as illustrated in figure 3.2. This dependency has numerous applications in many kind of optical systems. [27] Especially around the so called quadrature

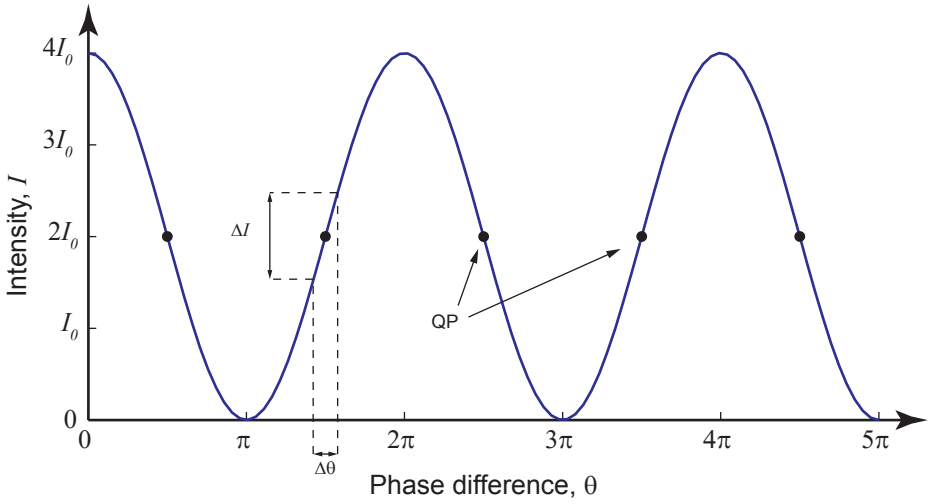

Figure 3.2. The calculated output of a photo detector during a scan of one mirror in direction of the beam, in a michelson interferometer. In this special case, $I_1 = I_2 = I_0$ makes the fringe visibility $V = 1$ and the resulting intensity varies between 0 and $4I_0$. If no interference would occur, the detected intensity would be $I_{DC} = I_1 + I_2 = 2I_0$. Interference with $V < 1$ will reduce the difference between I_{min} and I_{max}. The sine curve is steepest a the quadrature points (QP) of the interferometer. At QP, a small phase variation $\Delta\theta$ produces the largest variation in observed intensity.

points (QP) at $\theta = \frac{\pi}{2} \pm \pi$, where the sine curve is at its steepest, a small variation of phase is responsible for the largest variation in intensity, see figure 3.2.

The scanning Michelson interferometer constructed at Aalto university optics and photonics group [2] [1] utilizes these quadrature points to detect very low vibration amplitudes down to one picometer in various ultrasonic devices. The layout of the interferometer is illustrated in figure 3.3. In addition to a traditional Michelson interferometer setup (figure 3.1), polarizing optics are used to direct the laser beam. The rapidly varying intensity of the interfering beams is recorded with a high speed photo detector. Since the frequency of the intensity modulation is equal to the known sample excitation frequency, a spectrum analyzer can be used for measuring the modulation amplitude at that specific frequency in the photo detector output signal. Around the quadrature point, the measured modulation amplitude is proportional to the vibration amplitude of the sample surface.

The lateral resolution of vibration measurements is increased by using a microscope objective for focusing the laser beam into a spot with a size of around one micrometer. A two dimensional image of these single pixel measurements is then acquired by scanning through the whole sample laterally with a translation stage. Additionally, the setup enables creating a map of the reflected light power across the sample, effectively resulting in a microscope image of the device (figure 2.3a). In the layout shown in figure 3.3, this measurement is done by slightly tilting one of the wave plates recording the intensity of the reflected beam with a photo detector.

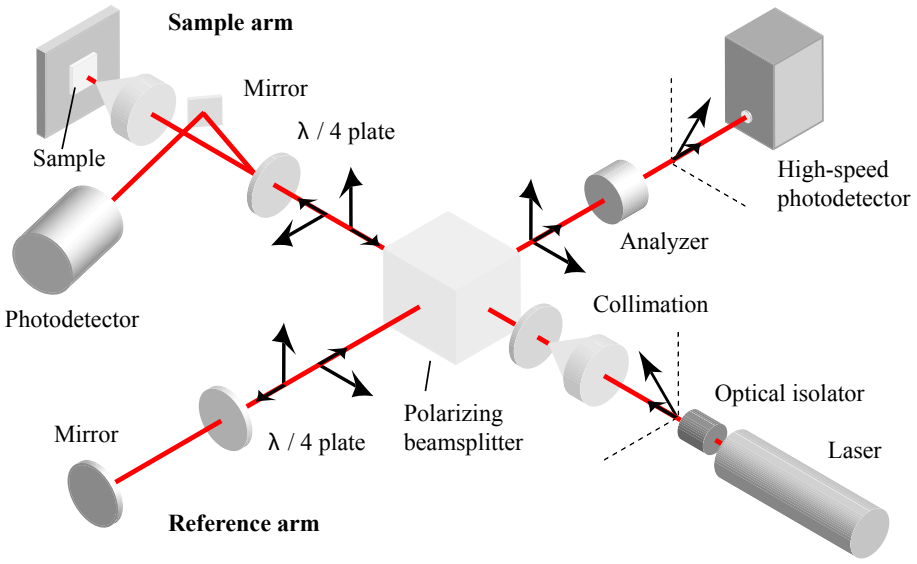

Figure 3.3. Layout of the scanning laser interferometer constructed at Aalto University optics and photonics group. A polarizing beam splitter and wave plates are used to direct the laser beam. The beam propagating direction is marked with small arrows. The big arrows denote the linear polarization direction of the beams. One pixel detection together with translating the sample is used for acquiring an image of the sample. Adapted from [1].

An example of a scanning laser interferometer measurement of a vibrating MEMS device together with its respective reflection map is illustrated in figure 2.3.

3.1.1 Imaging interferometry

The equations presented above only account a one-dimensional case, where the intensity of the resulting beam depends only on a single phase difference θ. This simplification is valid in situations when θ remains constant in the transverse imaging plane. This is the case when the incident waves are two parallel plane waves or wavefronts which have an equal radii of curvature, like spherical waves or two matching Gaussian beams. [26] Then the light beam shape will dictate the intensity profile which will then oscillate uniformly according to the changing θ in equation (3.4). If the beam intensity is recorded only in a single pixel, a two-dimensional measurement image cannot be obtained without scanning the beam and combining several measurements.

In a more general case, the curvature and tilt of the wavefronts does not match and both the phase difference θ and intensity $I(\theta)$ will depend on the lateral position (x, y). This will create an interference pattern which can be observed with a screen or an imaging sensor at the image plane. In this case, the observed pattern can consist of straight or circular fringes, as illustrated in figure 3.4.

This pattern carries information of the phase difference between the two wavefronts

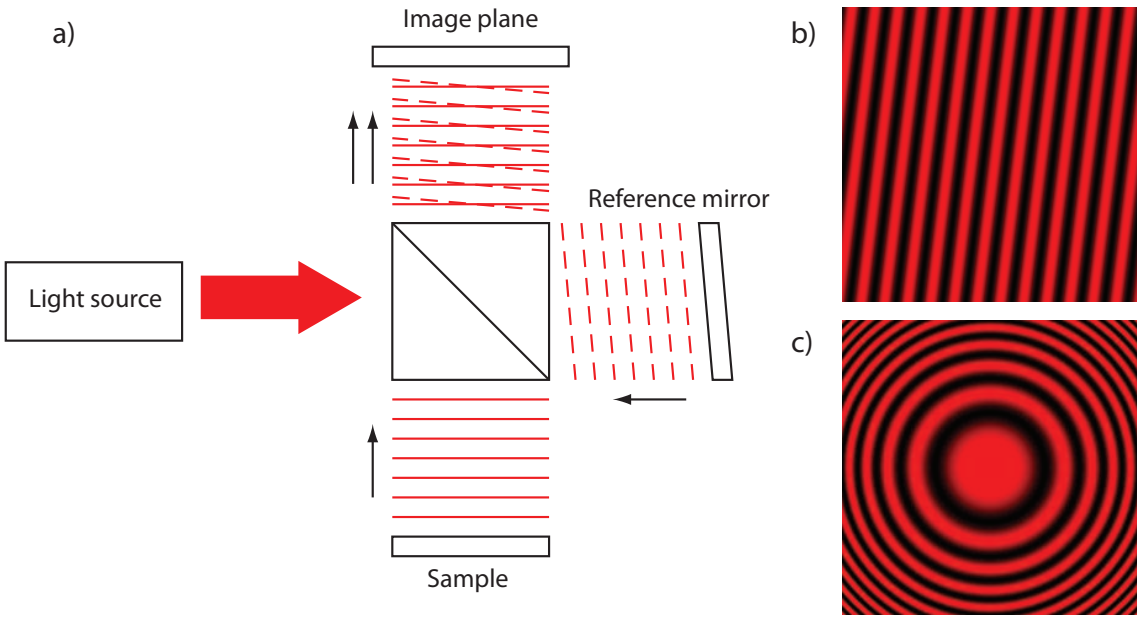

Figure 3.4. Operation principle of an imaging Michelson interferometer. **(a)** The light source delivers a wide beam of coherent monochromatic light spanning the width of the area to be imaged. For simplicity, the incoming wavefronts are not illustrated. Here the wavefront reflected from the reference mirror is slightly tilted with respect to the sample reflection wavefront. When the waves interfere, a fringe pattern is observed at the image plane. **(b)** The simulated fringe pattern of two planar wavefronts with unequal tilt. Each bright fringe corresponds to a phase difference of an integer number of wavelengths between the waves. Dark fringes correspond to half-wavelength phase differences. **(c)** An example of an simulated interference pattern between a planar and a spherical wavefront, achieved by replacing the planar sample mirror with a convex surface such as a convex mirror or ball bearing.

in all lateral (x, y) positions across the transverse plane inside the illumination beam. If the reference mirror is assumed to be perfectly planar, the pattern actually depicts the contour lines of the topography of the sample surface. Each bright line corresponds to a height difference of $\lambda/2$ (because of the Michelson geometry) on the sample surface, with λ being the illumination wavelength.

Whether the consecutive fringes represent contour lines that are higher or lower, can be concluded by making assumptions about the geometry of the topography, but the distinction is by no means self-evident. Identifying contours is essentially impossible especially with surfaces featuring discontinuations, such as discrete step profiles larger than half a wavelength. On these surfaces, the fringes break apart and can not be traced and matched with each other. This problem of distinguishing between hills and valleys is called the 2π ambiguity and is a major drawback of using monochromatic interferometry for topography measurements of profile heights spanning multiple wavelengths.

Now, in the situation of figure 3.4b, when translating either the sample or the ref-

erence mirror in direction of the optical axis z, the fringe contour lines are observed to move. When observing the intensity at a single point on the image plane (e.g. the signal of a single pixel of an imaging sensor) during the axial scan, an identical oscillation as described in the one-dimensional situation by equation (3.4) and illustrated in figure 3.2 is seen. This fringe pattern is observed in any single pixel on the imaging plane when modifying the phase difference, regardless of wavefront tilt or what the fringes look like in the image.

3.2 White light interferometry

Many interferometric applications, including those described above, require a light source with high coherence, i.e., a spectrum as narrow as possible. In white light interferometry, however, this concept is completely reversed.

Let's consider working with a light source emitting multiple wavelengths, all almost equal, used in the same interferometric setup as above. As with figure 3.2 depicting the pattern of a single wavelength, every wavelength present in the light beam will trace out a similar oscillating intensity pattern depending on the position of the translated mirror. However, the wavelengths of these oscillating patterns slightly differ from each other corresponding to the different wavelengths of the light source.

The signal detected at the monochromatic photo detector is the sum of all these intensity patterns, but their fringes coincide only near the point of zero optical path difference. Further away different fringes overlap and fringe visibility decreases (figure 3.5). Far away from the zero point, the components of different wavelengths lack mutual temporal coherence and a flat background intensity is observed.

Moving on to a more general case, instead of being a combination of individual wavelengths, the light source emits a continuous spectrum centered at a mean wavelength λ_0 and has a spectral bandwidth of $\Delta\lambda$ around it. Now the observed signal can be described as an integral over all sinusoidal fringes for all continuous wavelengths. [28]

Now, the fringe visibility V (equation (3.8)) is no longer a constant value but varies with z, since I_{min} and I_{max} also depend on the z position. This factor of variable visibility is called the *fringe envelope function* $\gamma(z)$ which replaces V in equation (3.10):

$$I(z) = I_{DC}\left[1 + \gamma(z)\cos\left(\theta\left(z\right)\right)\right], \tag{3.11}$$

where the fringe oscillation depends on

$$\theta(z) = 2k_0 z = 2\frac{2\pi}{\lambda_0}z, \tag{3.12}$$

with k_0 being the central wave number corresponding to central wavelength λ_0. The factor 2 comes from the Michelson interferometer geometry, where a mirror displacement z results in a round-trip optical path difference $2z$.

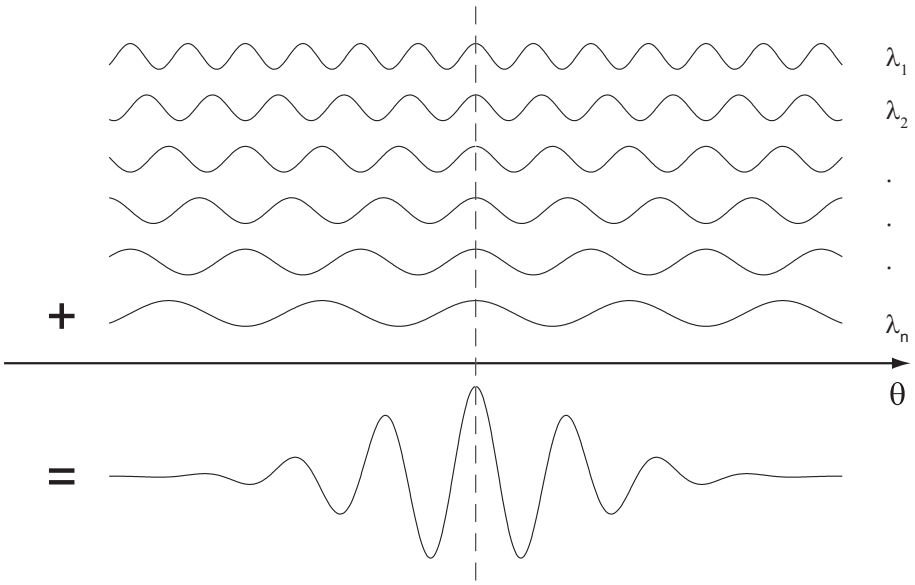

Figure 3.5. Formation of the white light interferogram. The light source emits light at several wavelengths. One mirror is translated axially, and the resulting intensity is recorded at the detector. Each wavelength creates an interference pattern in the form of a sine wave as a function of phase difference, as in figure 3.2. The intensity detector is unable to distinguish the colors from each other and only records the sum of all the patterns. At the point of matching interferometer arm lengths, i.e. zero optical path difference, the fringe patterns coincide and fringes are seen in the detected signal. Outside the zero OPD point the light waves become mutually incoherent, their fringe patterns overlap and the detector only records constant shades of gray. For simplicity, only six waves are illustrated here. In reality, an interferogram like depicted here is an integral over a wide spectrum of continuous wavelengths.

The fringe envelope $\gamma(z)$ determines the location of visible fringes wherever it deviates from zero. Therefore the envelope shape is an important factor in determining the tolerance for how long the optical path difference can be while still producing observable fringes.

The shape of the fringe envelope can be calculated from the light source spectrum using a Fourier transform. [28] [29] Irregular source spectra, as well as other factors like spectral sensitivity of the detector or camera, material and wavelength dependent phase change on reflection and dispersion in the optical system have effect on the resulting interferogram shape. For the simplified case of a gaussian source spectrum, the envelope of the fringes will also be a gaussian function. [27] For a gaussian spectrum with central wavelength λ_0 and bandwidth $\Delta\lambda$, the width of the envelope, the *coherence length* is

$$l_c = \frac{2\ln 2}{\pi}\frac{\lambda_0^2}{\Delta\lambda}. \tag{3.13}$$

Here, both $\Delta\lambda$ and l_c are defined as the $1/e$-width of the gaussian function, i.e., the

width of the interval inside which the function has a value greater than $1/e \approx 37\%$ of its maximum.

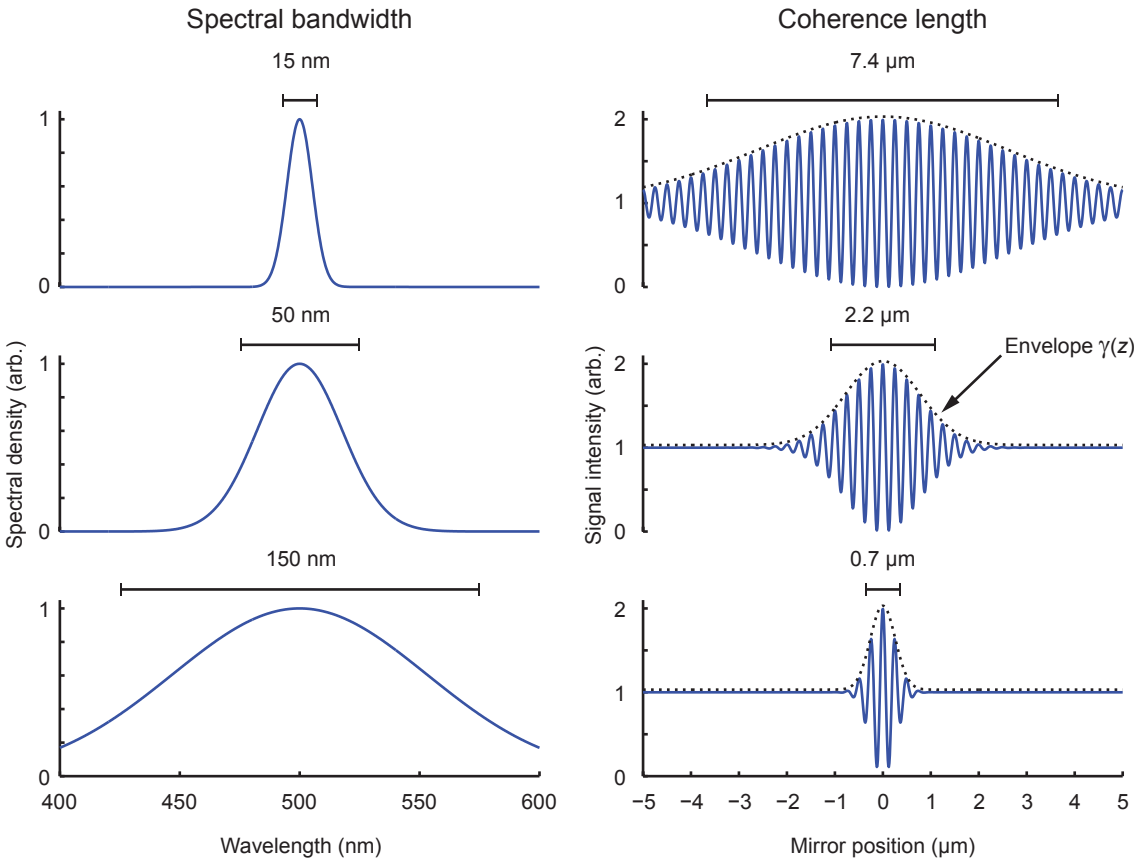

Figure 3.6. Effect of the light source spectral width on the coherence length. Left column shows the spectra of three different light sources. In the right column are the corresponding intensity signals observed at the detector when altering the optical path difference. The envelope which modulates the oscillating interference signal is drawn with a dashed line.

A wider light source spectrum results in a shorter coherence length. An ideal monochromatic source would result in an infinite coherence length, but real life highly monochromatic light sources like good quality frequency-stabilized Helium-Neon laser can have a coherence length exceeding one kilometer. Non-stabilized HeNe-lasers have a coherence length of around 30 cm, which is still very suitable for the typical Michelson interferometers, and even some interferometer configurations which feature uneven path lengths. The wider emission peaks of diode lasers result in a coherence length of just a few millimeters. [26] [27]

Using light sources with large bandwidths like LEDs and halogen lamps or even white light tungsten bulbs will give a very narrow coherence length of even less than a few micrometers. This means that even these kind of light sources, which are normally considered unsuitable for interferometry, will produce observable interference fringes as long as the dimensions of the interferometer match. White light interference and

the effect of narrow coherence is illustrated with actual photographs in figure 3.7.

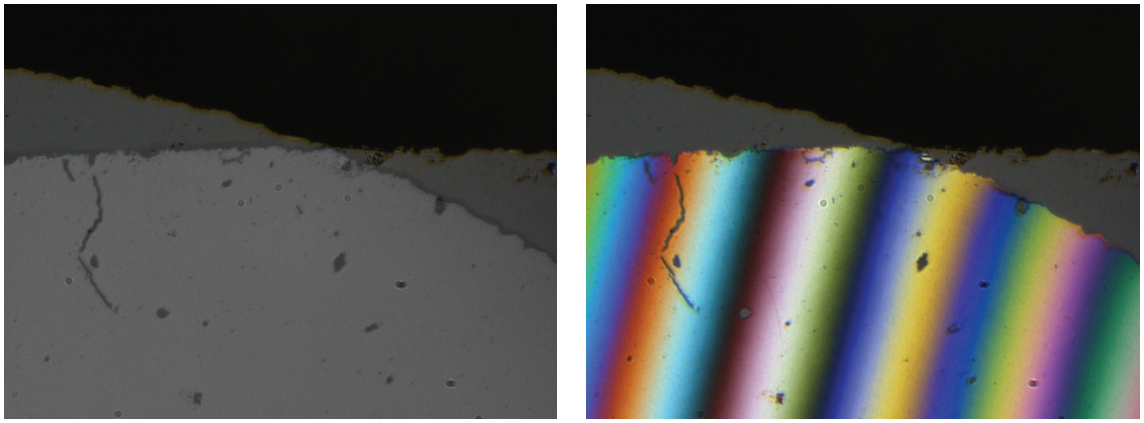

Figure 3.7. Demonstration of interference using a white LED as a low-coherence light source. In an imaging Michelson interferometer, edges of two planar mirrors are superimposed in the image frame. In **(a)**, both images appear sharp since they are within the depth of field, but no interference is observed. In **(b)**, while still within depth of field, the mirror distances are matched within the accuracy defined by the coherence length and interference fringes appear.

The low coherence of white light can be turned into an advantage by making use of the information that the short coherence region withholds: When detecting interference, the measurement arm length is guaranteed to be equal to the reference arm length with an accuracy defined by the coherence length. If the reference mirror can be displaced by small, known amounts, like with a motorized translation stage, differences in height of the reflective surface on the measurement arm can be measured without ambiguity.

A beautiful representation of a white light interferogram can be produced in the geometry of figure 3.4 (a) and (b). Tilting the two mirrors results in a patterns of straight fringes across the image, perpendicular to the direction of tilt. As described, translating either mirror axially makes the fringes move in the direction of tilt. When monitoring a single pixel on the image plane, the bypassing fringes trace out the familiar sine curve when the intensity oscillates. This means that the same pattern detected in a single point can be visualized as a two-dimensional image.

A comparison simulation between monochromatic red light and low coherence white light interference in this geometry is illustrated in figure 3.8. The white light frame shows that the fringes are not like an ever continuing sine function, but are very localized and only show up when the intersection of the two planes is within the field of view. The colored simulation also shows the actual appearance of a white light interferogram: when fringes of different color are spaced apart different amounts, the resulting fringes appear colored like a rainbow.

Furthermore, even if the variation in intensity fades away very quickly, alternating

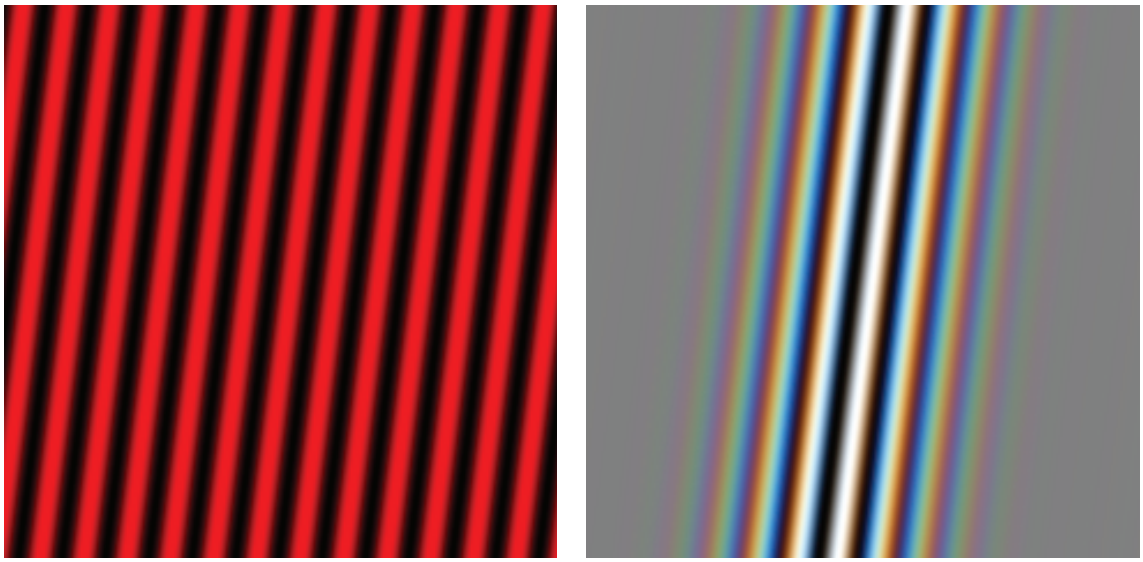

Figure 3.8. Simulated outputs of an imaging Michelson interferometer with two slightly tilted planar wavefronts. **(a)** uses highly coherent monochromatic red light, and periodic interference fringes are observed throughout the frame. In **(b)**, white light of low coherence is used, and interference is only observed around the line where the wavefront planes intersect. Elsewhere, the optical path difference increases, fringes of different colors overlap and the pattern washes out. The interferometer geometry is illustrated in figure 3.4 (a). The red fringe pattern in (a) is the same as in figure 3.4 (b).

colors can be seen with a device capable of delivering color images, such as a color sensor camera or the human eye. The red, green and blue colored components of the image represent a narrower portion of the light source spectrum, which increases the coherence length, i.e., enhances fringe visibility away from the zero point. Converting the image to grayscale is equivalent of using the whole light source spectrum (or, to be more precise, its combination with the camera sensor sensitivity).

Now, suppose that initially, the reference mirror is close to the beam splitter and it will gradually be translated away from it. At regular intervals during the translation, an image is recorded at the detector arm. As described, interference is observed in a single (x, y) location once the sample surface distance at that point is within the coherence length away from the reference mirror distance. Fringes are first detected at the edge where the tilted sample surface is higher. The fringes then travel across the image and vanish at the lower edge (figure 3.9).

The fringe pattern can be thought of as a narrow set of elevation contour lines that travel through the sample surface from top to bottom, as illustrated in figure 3.10. In the sequence of recorded images, the intensity of a single pixel (x, y) traces out the interferogram pattern, when plotted as a function of the corresponding reference mirror position. For each pixel, the central position of the fringe pattern can be

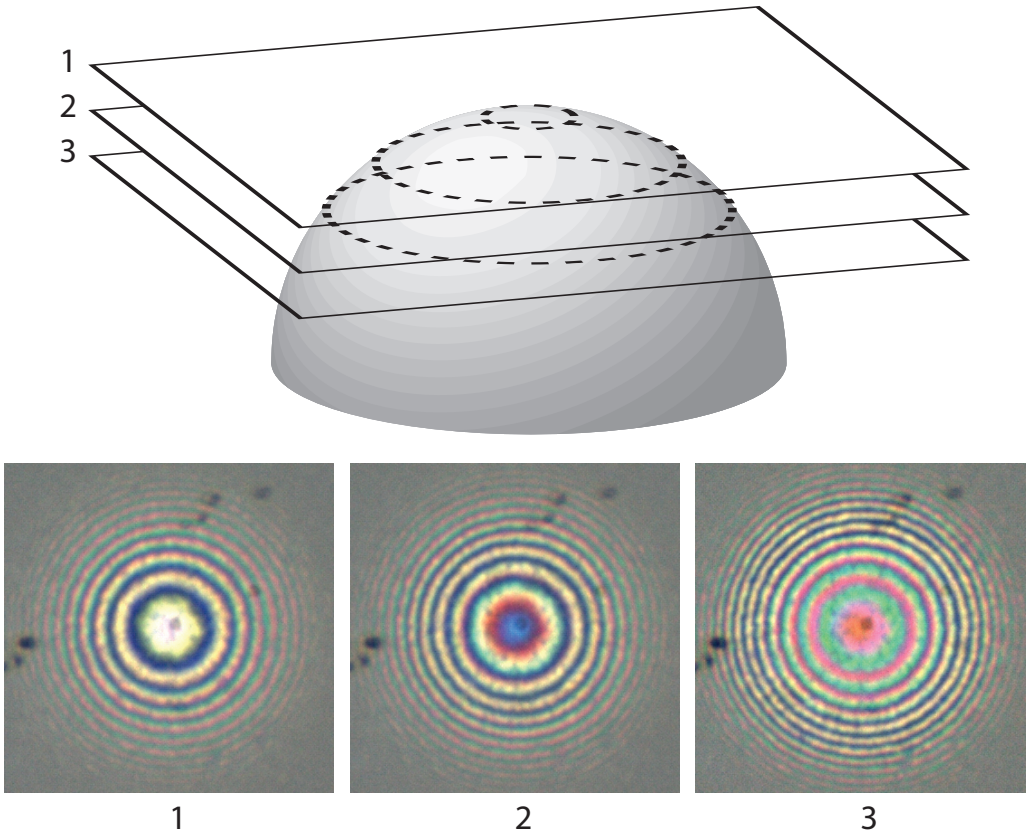

Figure 3.9. White light fringes appear along the intersection of the reference distance plane and the sample surface. The three images show interference on a steel ball bearing, with the reference surface level descending between each frame.

determined using digital signal processing techniques. This central point defines the surface height at the location of each pixel, and can be used to create a three-dimensional surface plot of a sample.

The term white light interferometry is commonly associated specifically with surface topography measurement applications. Other frequently used terms include vertical scanning interferometry (VSI), low coherence interferometry (LCI), coherence probe microscopy and interference microscopy. Interferometry using white light also has other partly related applications. In life sciences, white light interferometry is used similarly as described above, but to probe transparent media, to create volumetric images of tissues, for example. This application is commonly referred to as optical coherence tomography (OCT). Fourier transforming recorded interferograms can also be used to reconstruct the light source spectrum, or if the illumination spectrum is known, the relative absorption spectrum of a sample between the light source and the interferometer. This application of white light interferometry is known as Fourier transform spectroscopy and often Fourier transform infrared (FTIR) spectroscopy.

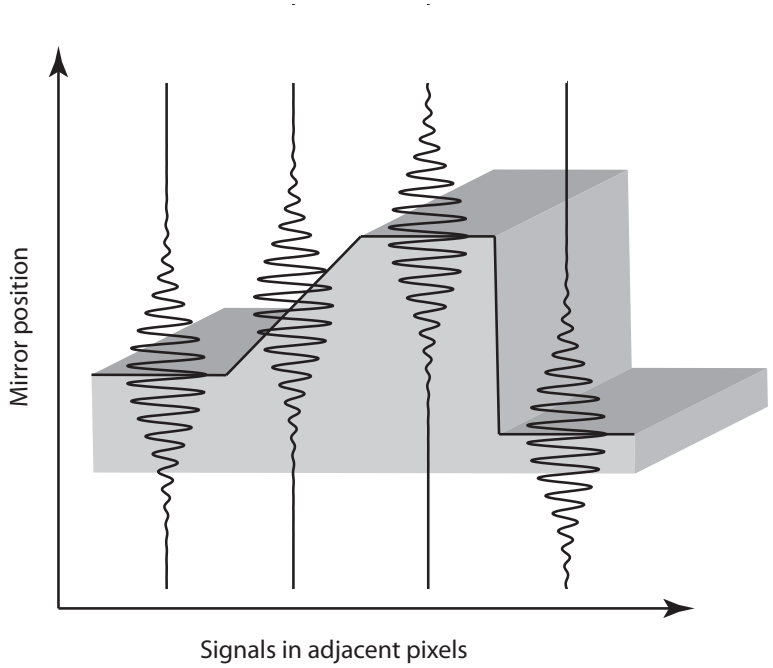

Figure 3.10. Individual pixels each trace out the interferogram pattern. At each pixel location, the sample surface height is found by locating the z value of the envelope peak.

Chapter 4

Experimental setup

4.1 Principle of operation

Previously, a microscopic imaging system with stroboscopic illumination was constructed as part of a special assignment [30]. The system is designed for acquisition of static microscopic images of MEMS resonators that experience in-plane vibration, i.e., lateral vibration perpendicular to the optical axis of the imaging system.

The devices of interest typically operate at frequencies below 1 MHz. Even while they are categorized as low frequency resonators, acquiring static images of them would require extremely fast shutter speeds well below 1 µs. Directly imaging resonators operating in the range of 1 kHz has been demonstrated with high-speed cameras capable of 32000 frames per second [21], but with the disadvantages of high cost, low resolution and inability to research devices of higher frequencies.

Very short exposure times are typically easiest to implement by using a longer shutter speed while illuminating the subject using a very short light pulse. However, submicrosecond light pulses require an impractically high amount of momentary light power. For comparison, the pulse duration of normal camera flash units only reaches down a few hundred microseconds. [31]

The problem of freezing very fast motion is overcome by exploiting the periodicity of vibration. If the sample is illuminated with short, repeating light pulses at the same frequency the sample is vibrating at, the sample will always be at the same phase of vibration when lit. The exposure time of the camera can then span even thousands of vibration cycles while the sample appears stationary in the recorded image (figure 4.1a).

By altering the phase difference of the signals driving the vibration and illumination, a sequence of images depicting different phases of the vibration can be acquired. In post processing, feature tracking and/or two dimensional cross correlation techniques are then used to extract a vector field of the lateral vibration from the recorded images at an accuracy of less than one pixel. [32]

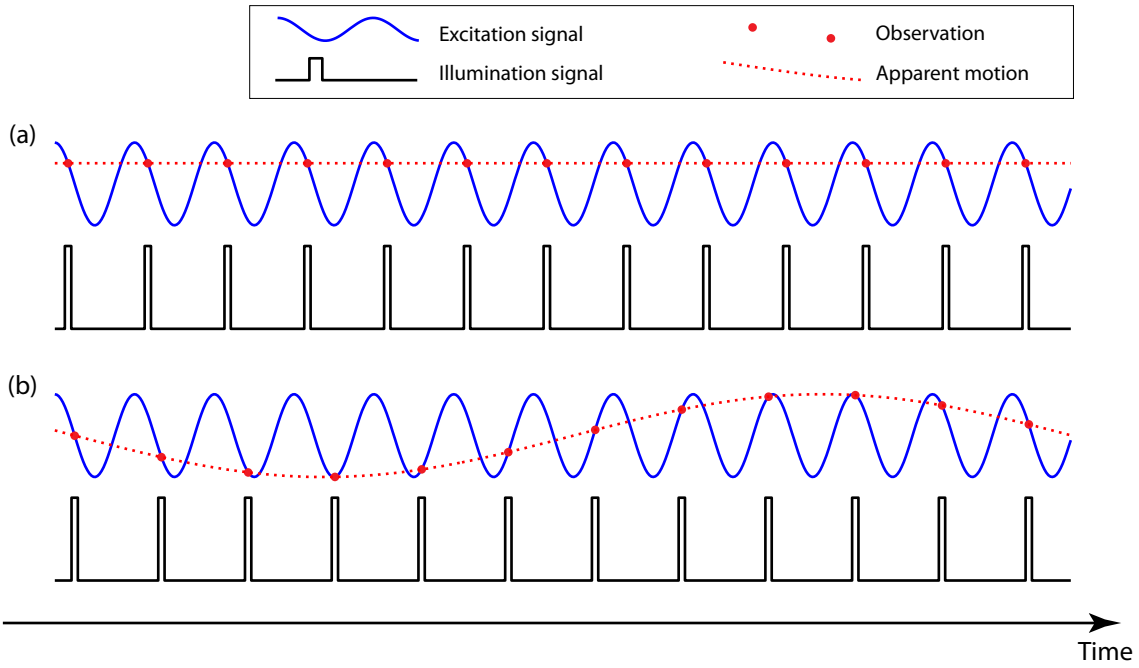

Figure 4.1. Principle of imaging with stroboscopic illumination. **(a)** The sample is driven with a sinusoidal excitation signal. Illumination is driven with a pulse which switches the light source on only for repeating, short periods of time. When the sample is moving at the same frequency that the illumination is driven at, it will always be at the same position when the light source is on. The camera exposure time can now be as long as necessary, while the sample appears to be stationary. **(b)** Introducing a slight frequency offset between the sample driving and light pulsing signals, the sample vibration will advance slightly before the next light pulse. This vibration aliasing will make the sample appear to vibrate very slowly, at a frequency equal to the difference between the two signal frequencies.

When watching a live video stream from a camera looking through the microscope, the vibration can be visualized in a convenient way by illuminating the sample at a slightly different frequency than the sample is vibrating at. This creates frequency beating, an aliasing effect realized as the sample appearing to vibrate at a very low frequency (figure 4.1b). This slow motion vibration is observed at an apparent frequency equal to the difference between the drive and illumination frequencies. A 1 Hz frequency offset is typically suitable for visualization purposes.

In this master's thesis, the in-plane vibration detection setup is extended to function as an imaging white light interferometer, capable of measurements of out-of-plane vibration as well. By splitting the illumination and adding a reference arm with a planar mirror, white light interference fringes are observed at locations where the sample surface height corresponds to the optical distance to the reference surface.

If the position of the reference surface is altered with a translation stage while recording a sequence of images, an interferogram like illustrated in figure 3.5 is acquired for every pixel. The location of strongest interference fringe contrast along

the z-axis at a single pixel then defines the surface height at that pixel.

With the above procedure, an interferometric imaging microscope with a scanning reference mirror can be used to measure a three dimensional surface profile of a stationary sample. The setup can then be extended even further to allow for measuring periodically deforming surfaces. When a pulsed light source is used and synchronized with the vibration, a measurement results in an apparently stationary three dimensional surface profile. Changing the phase offset of the signals again produces measurements of different phases of the vibration period. A sequence of profile measurements with different vibration phase values can then be used to reconstruct a three-dimensional animation of the motion of the device under study.

4.2 Hardware

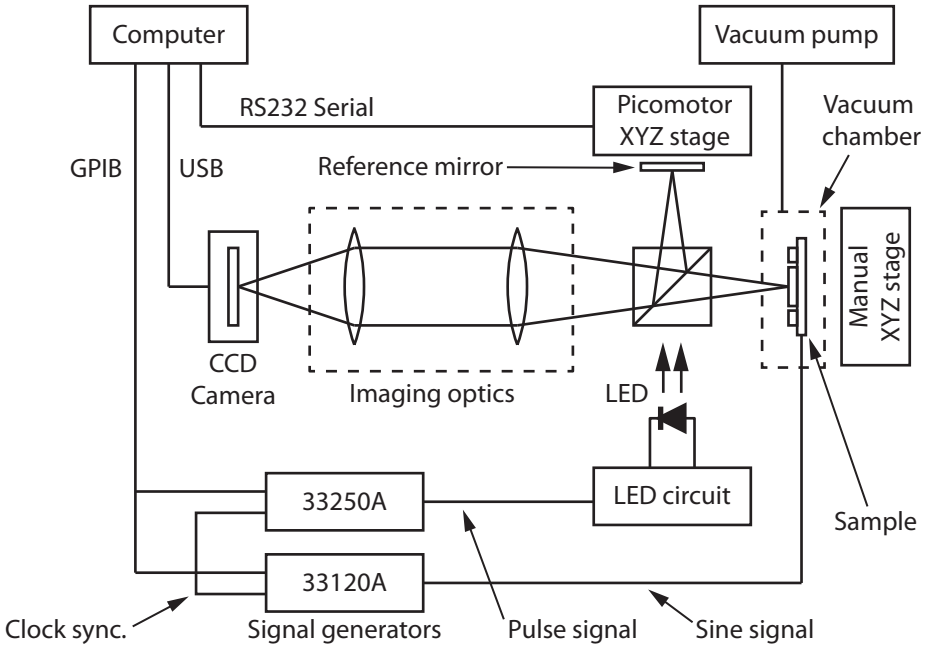

Figure 4.2. A block diagram of the measurement setup. LED illumination is divided to the sample and the reference mirror using a Michelson interferometer layout. Images of both surfaces are overlaid and projected on the sensor of a CCD camera, which is used for observing the interference between the light fields. Computer controlled signal generators are used to synchronize short illumination pulses with the excitation signal of the sample. The sample is positioned and focused manually, while the position of the reference mirror is swept with a motorized translation stage for obtaining a set of white light interferograms. A vacuum system is used to control the effect of air pressure on the vibration behavior of the sample.

Figure 4.3. Volpi AS11/50 video microscope probe. A C-threaded mount for the camera is at the right. The long narrow tube extruding to the left houses the front lens element. The front lens is surrounded with optical fibers for coaxial illumination. The perpendicular illumination port for interfacing with a light source is at the back. Focusing is carried out with knurled focuser ring in the middle.

4.2.1 Optics

Imaging optics

A C-mount Volpi 50mm f/11 video microprobe (AS11/50) lens (figure 4.3) is used for the imaging optics of the setup. The standard C-threaded mount can be used to connect the lens to various industrial digital cameras. The lens houses an illumination port using a bundle of optical fibers from the port to an annular shape around the perimeter of the front lens element. Much like a photographic ring flash, it creates a uniform, diffuse illumination which is suitable for imaging rough or uneven surfaces.

For imaging flat, polished surfaces like those on MEMS resonators, using the illumination port is not ideal. When focused on a flat reflecting surface, the illumination appears as a defocused reflected image of the front lens perimeter, which is twice as far behind the sample surface from the actual front lens element. The field of view of the camera is completely inside the image of the defocused annular shape. This results in the flat surface appearing totally dark, with diffuse features like dust spots appearing very bright. Imaging the reflected light is only possible by tilting the sample surface so that the edge of the annulus appears in the field of view, making the illumination port unsuitable as a light source for interferometry. Instead, illumination is delivered via the beam splitter in front of the objecitve.

The Volpi microscope probe achieves an optical magnification factor of slightly less than 5:1, i.e., the linear size of the image projected on the imaging sensor is five times larger than the size of the actual object. Given the 4.65 μm pixel size of the sensor (section 4.2.2), this combination results in a scale of roughly 1.05 μm per pixel, which in turn makes the field of view roughly 1.3 mm x 1.0 mm. To achieve the highest magnification factor and keep it from changing, the focusing scale on

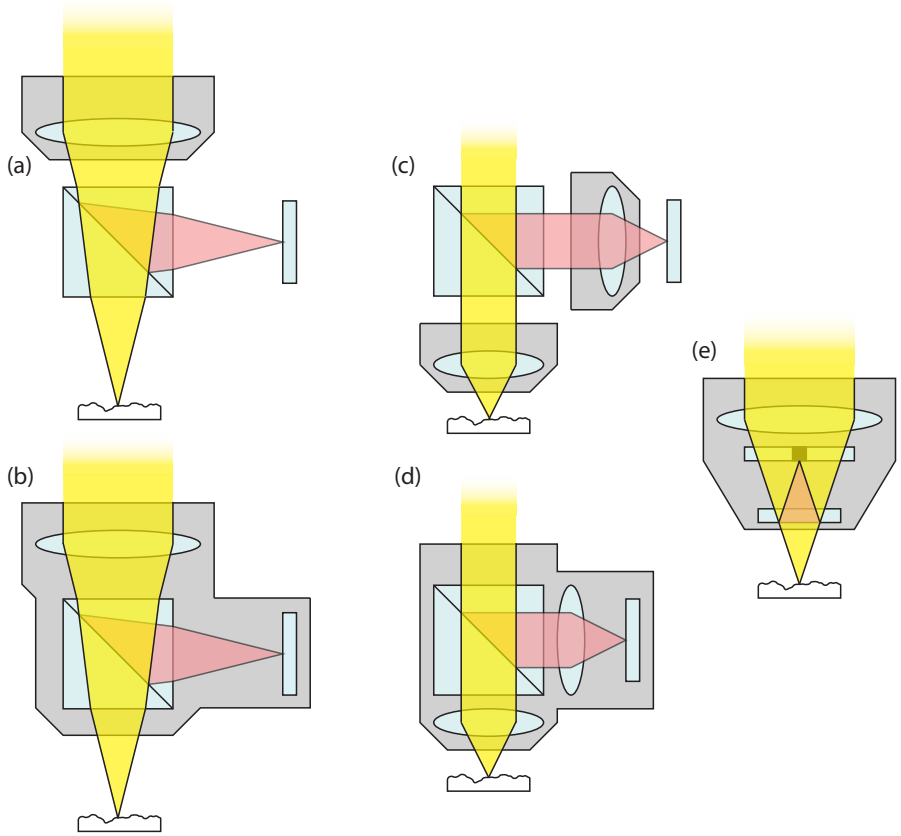

Figure 4.4. Various interferometric microscope configurations: **(a)** Michelson **(b)** Enclosed Michelson **(c)** Linnik **(d)** Enclosed Linnik **(e)** Mirau.

the Volpi lens is left at its closest focus setting. The focusing is then carried out by moving the sample in the Z-direction (see section 4.2.7).

Interferometer optics

Equipping an imaging interferometer (figure 3.4) with microscope optics for greater magnification can be done in various ways. Some common configurations are illustrated in figure 4.4. A Michelson interferometer can be assembled in the front of the imaging lens (a). A high power microscope objective, however, normally prevents this because of the limited working distance available between the lens and the object. The beam splitter can also be behind the objective, but for best performance in this configuration, the reference arm also needs to be equipped with an identical lens. A Michelson configuration with objectives on both the measurement and reference arms (c) is referred to as a Linnik interferometer. [27]

Both of these configurations require careful collimation for all components to be coaxial both in position and tilt. For the interferometer to be as unsusceptible to vibration as possible, components also have to be very solidly fastened in place. Objective modules enclosing a Michelson or Linnik interferometer (b and d) are

also available. Another even more compact solution is the Mirau objective (e), in which a thin planar glass acts as the beam splitter. The reference mirror is a small aluminized spot on another glass plate, or sometimes on the front surface of one of the microscope lens elements. These specialized objectives lack the need of collimation and make the optical system very robust and sturdy, but they also come with considerable cost. Another disadvantage is that they need the illumination to be coaxial and be introduced to the optical path before the lens module. In the orientation of figure 4.4, the light has to come from above, which would require an additional beam splitter or other means of light output along the optical axis. In the open configurations (a) and (c), illumination can be delivered from the left via the beam splitter, which divides it into the sample and reference arms.

Since the Volpi microprobe offers a generous working distance of 60 mm, it allows assembling a basic miniature Michelson interferometer between the lens and the sample. Because of this and the ease of illumination, configuration (a) was chosen for assembling the setup.

A 20 mm cubical beam splitter is used for splitting and combining the light. No polarization control is used in the interferometer, so the beam splitter is of non-polarizing type. The beam splitter is situated in front of the microscope probe head, about 30 mm above the sample surface. A reference mirror is located on the side of the vertical optical path at the same distance of about 30 mm from the beam splitter. For preventing the reference mirror to introduce any systematic error to the reference wavefront, a precision planar mirror with $\lambda/20$ wavefront accuracy is used.

4.2.2 Camera

The camera used is a DFK41BU02 USB camera by The Imaging Source (figure 4.5) using the Sony ICX205AK Color CCD sensor [33]. The sensor format is 1/2" with a size of 7.6 mm by 6.2 mm. The size of a single pixel is 4.65 µm and the total resolution of the image is 1280x960. The camera is capable of an uncompressed RAW-format video stream at 15 frames per second.

CCD and CMOS imaging sensors used in digital cameras are arrays of elements that cumulatively record the incident light intensity falling on them. As such, they lack the ability to separate wavelength information of the photons they gather, i.e., typical imaging sensors actually only produce black and white images. For acquiring a colored image with red, green and blue color channels, the incident light needs to be filtered before being recorded in the pixels. Using colored filters to capture three different images and combining them together results in a color image, but will generally be inconvenient to capture and unsuitable for imaging moving objects.

One shot color (OSC) cameras solve this problem by using a color filter array (CFA) in front of the imaging sensor. [34] The array consists of a pattern of very small color filters in front of each individual pixel. The intensity of each pixel then contains

Figure 4.5. The Imaging Source DFK41BU02 USB CCD camera. The CCD image sensor is visible inside the C-threaded lens mount in the front. The camera can be mounted using one of three 1/4" UNC or one M6 threaded holes in the bottom. In the back, a BNC trigger port and a USB data port are available. The camera operates at the USB 5 V voltage and requires no external power supply.

information of one color. A suitable interpolation algorithm [35] is then used to reconstruct each pixel with the information of its missing color channels, based on the measured values of neighboring pixels.

The most common color filter array for arranging RGB colors on a square grid of pixels is the Bayer matrix [36]. It has repeating 2×2 pixel blocks in an RGGB arrangement with green filters covering 50% of the total number of pixels. The Bayer color filter array and its color interpolation work flow is illustrated in figure 4.6. A Bayer matrix is also used on the color sensor of the DFK41 camera.

While using a one shot color sensor is convenient for acquiring colored images, drawbacks also exist. The most obvious disadvantage is the loss of spatial resolution. Reconstructing the two thirds of missing data for the color channels of each individual pixel can be thought of as using a red, blue and two green images captured at half resolution and sampling them up to acquire the final colored image. A second drawback is the reduced light sensitivity of the sensor, since roughly two thirds of incident photons are discarded by the color filters. A monochromatic camera also produces data files one third the size compared to colored data, which will save hard drive space and simplify post processing of the data.

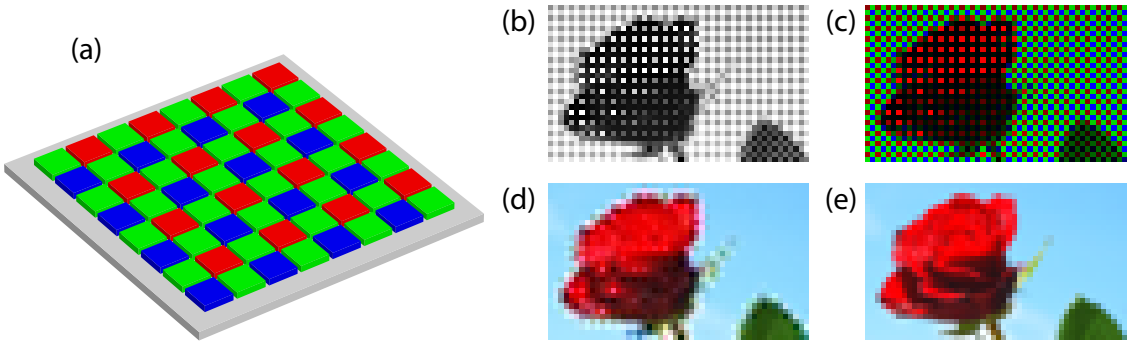

Figure 4.6. **(a)** Illustration of an image sensor with a Bayer color filter array. Each pixel is covered with either a red, green or blue color filter. **(b)** Raw black and white image data from the sensor. The filter array leaves a distinct checkerboard pattern across the image. **(c)** Each pixel marked with its respective color. **(d)** Demosaiced image with missing color values interpolated from neighboring pixels. **(e)** Original full RGB image used in generating the examples. In this case, the combination of very low spatial resolution with a rudimentary interpolation algorithm is unable to accurately reconstruct the contents of the original image.

However, color sensors can also be beneficial in certain circumstances. Imaging optics with perfect or nearly perfect color correction are very expensive. Imperfect color correction results in the focal planes of different wavelengths being at different distances. This problem typically manifests itself in the blue image not being in focus simultaneously with the red and green channels. In high contrast images, bright features against a dark background appear to have a blue halo around them. The contrast of images of uniform scenes will be degraded by a bluish haze or glare evident throughout the image.

In this case the red and blue color channels can be discarded. The green channel only needs interpolation of every other pixel and whether this is a problem or not depends on the combination of resolving power of the optics and the sensor, as well as the scale of details that are to be imaged.

Furthermore, the shape and width of the interferogram (section 3.2) depend on the combined effects of the spectral sensitivity of the camera sensor, the color filter pass band shape and the spectral output of the light source. If only the green channel is selected for processing, compared to the situation of imaging with a monochromatic sensor with no color filter array, the spectrum of a white light source is effectively narrowed down. Depending on the the light source and color filter spectra, a more gaussian shape of the combined spectrum can be beneficial for the quality of the measured interferogram and the surface measurement accuracy.

4.2.3 Signal generators

For stroboscopic imaging of sinusoidally moving samples, two signal generators are needed. The studied MEMS devices are typically excited with a sinusoidal input

signal and show a linear vibration response. This sinusoidal vibration can then be imaged by illuminating the sample with short periodic light pulses matching the vibration frequency (see section 4.1).

The sample is driven by a sine wave generated with a Hewlett-Packard (HP) 33120A 15 MHz function generator. The amplitude of the sine signal depends on the MEMS device, typically being less than 1 volt peak to peak. Some devices utilizing capacitive coupling [15] require an additional bias voltage, often around 10 volts.

An Agilent 80 MHz 33250A signal generator feeds the illuminating LED trough interface electronics with short square pulses at the matching frequency. The generators are synchronized with a 10 MHz reference clock.

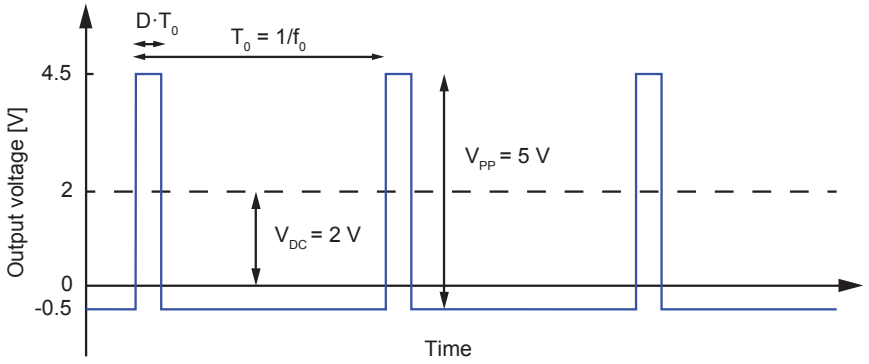

Figure 4.7. Voltage levels of the output by the pulsing signal generator. The meaning of the signal generator parameters V_{PP} and V_{DC} is illustrated.

4.2.4 Pulsing electronics

A simple switching circuit is used to interface the pulse signal generator output with the LED. The LED is connected to a 12 volt power supply unit with a 50 Ω bias resistor. A BS170 MOSFET transistor with rise and fall times of 10 ns is used to switch the LED on when a square pulse is received from the signal generator. The electronic circuit is illustrated in figure 4.8.

A suitable level for the high value of the pulse generator output is around 5 volts. To make sure the MOSFET switches the LED on only during high pulses, the low value is set slightly negative. The generator is set to deliver a V_{PP} (peak-to-peak voltage) of 5 volts with an offset voltage V_{DC} (average of high and low voltages) of 2 volts. This results in a voltage swing between -0.5 V and 4.5 V (figure 4.7).

The illumination circuit performance can be characterized by measuring the LED output pulse shape with a photo diode and an oscilloscope. Measured output pulses show that the led intensity is convoluted with rounded leading and trailing edges, when compared to the square control pulse. The leading and trailing edges of the

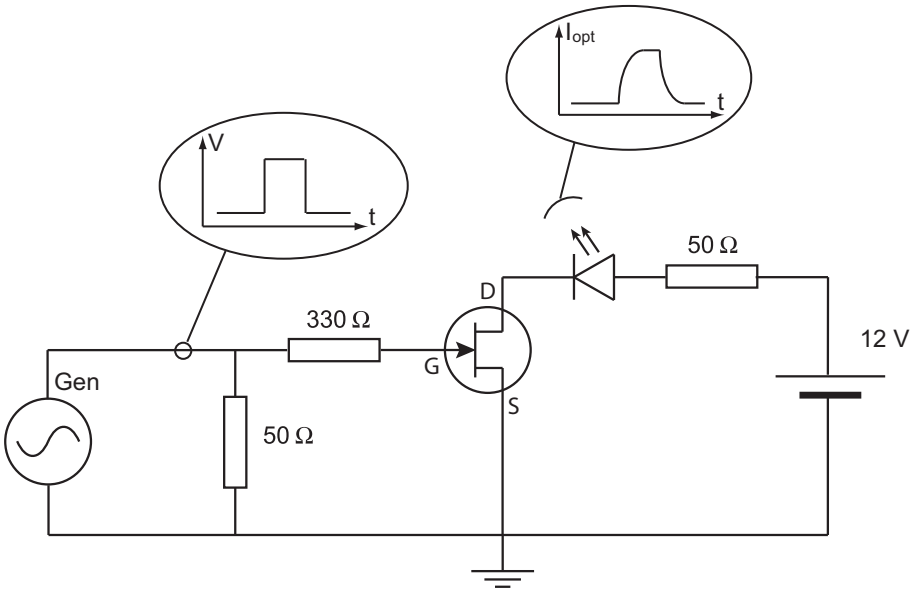

Figure 4.8. Schematics of the electronic circuit used for controlling the LED via a square pulse generator. The pulses are fed to the gate of the BS170 MOSFET, which switches on the 12 volt LED circuit at the right hand side. Also shown are the voltage level of the square pulse and the corresponding, convoluted pulse of the light intensity as functions of time, both in arbitrary units.

square control pulses show a very slight amount of ripple when examined in an oscilloscope. The ripple does not show in the LED output.

Intensity measurements of the LED output intensity with a range of different control pulse lengths are illustrated in figure 4.9. The output intensity increases rapidly for approximately 400 nanoseconds after the leading edge of the square control pulse. After this, the intensity continues to increase at a reduced rate for several microseconds. Thus the trailing edge of pulses shorter than 400 ns begins to fall down before before the rapid rise of the leading edge is over. The light power of a single pulse, i.e. the integrated area of the pulse curve, decreases fast when making the pulse shorter. The lack of light power hinders the usage of short pulses that are needed for stroboscopic imaging of higher frequency devices. However with a capable camera, the loss of light can simply be compensated by selecting a longer exposure time for a single image frame. This however has the drawback of extending the total duration of a measurement run.

A suitable length of a single light pulse depends on the operating frequency of the device to be measured. During pulsing, the fraction of time the light source is on is called the *duty cycle*. This percentage governs the total output and apparent brightness of the LED, so increasing the duty cycle will shorten the exposure time needed for a single frame and thus decreases the total duration of one measurement run.

Using longer pulses has the disadvantage of decreasing phase resolution of the mea-

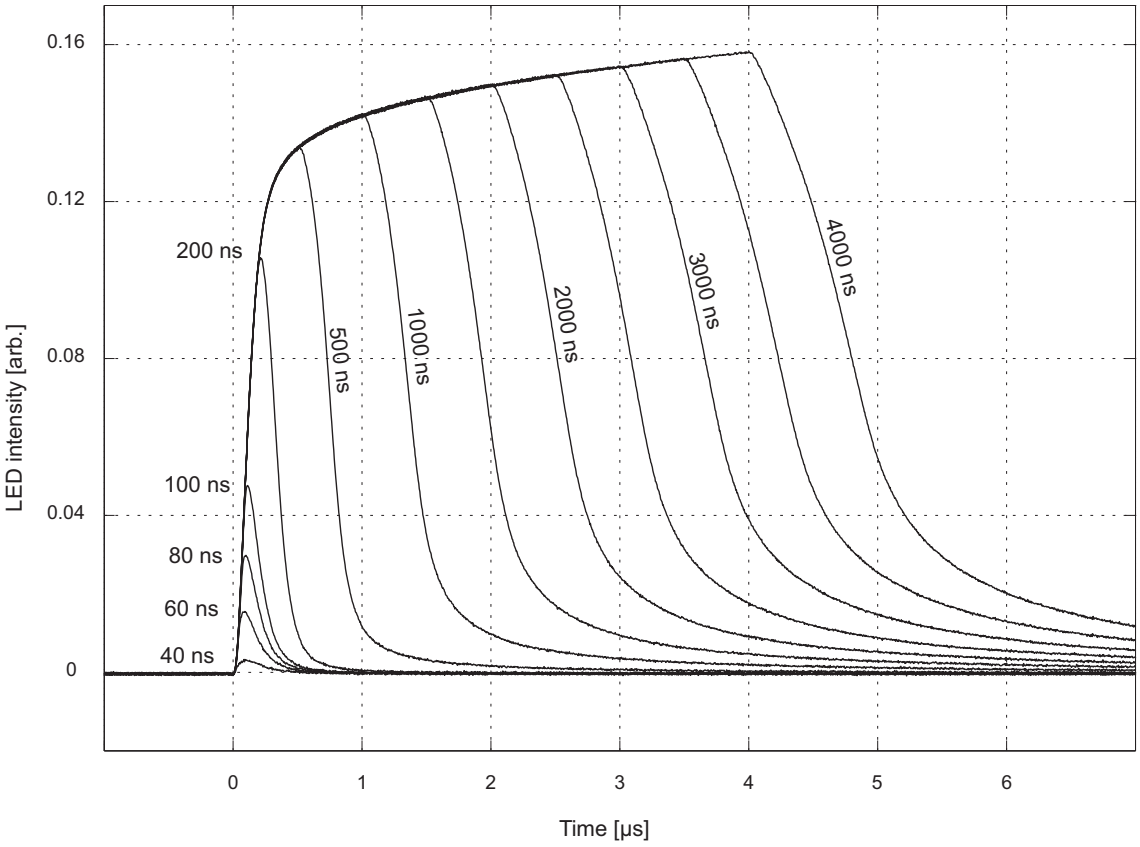

Figure 4.9. Measurements of the LED output with different control pulse length settings. The pulses show a rapid rising edge which is entirely contained within pulses longer than 500 ns. After this, the intensity continues to rise at a slower rate. The falling edges show similar behavior.

surement. A too long light pulse has the same effect on the measurement than a long shutter speed has in a photograph of a rapidly moving subject: motion blur will be visible in the exposure.

Another restriction is the current tolerance of the light source. During the short light pulse, the specified maximum continuous current of the LED can momentarily be exceeded by a very large factor. Because of this, LED is used with a current limiting resistor with much less resistance than needed when connecting an LED to a constant 12 volt power supply. A too high duty cycle might then result in the total time averaged current flowing through the LED becoming too large and damaging the light source.

In practice, a duty cycle between 1/100 and 1/20 is optimal for stroboscopic measurements, being long enough to provide enough illumination but not too long to cause significant motion blur. If operating at a frequency around 10 kHz, a duty cycle of this magnitude produces light pulses with lengths from 1 up to 5 microseconds. By choosing a light pulse as short as 50 ns and a duty cycle of 1/5, a strobe frequency of 4 MHz is achieved, which is probably a good estimate for the highest

measurement frequency of the current illumination setup. A more sophisticated, operational amplifier based pulsing circuit operating with a normal LED has been demonstrated to achieve 10 MHz strobe frequencies. [37]

4.2.5 Light sources

Various white light sources of low coherence, such as light bulbs or LEDs can be used for illumination. These sources have different spectra and thus create different fringe envelopes. A wide-band light source creates a narrow envelope which allows determining the location zero path length difference with better accuracy.

In setting up the interferometer, using a red semiconductor laser diode was found to be convenient in roughly aligning the optical components. With its coherence length in the order of millimeters, the diode makes it easy to observe interference fringes, but still aids in matching the optical path lengths of the interferometer arms. In addition, running a laser diode with a supply voltage below its lasing threshold, the spectral line width of the laser's emission becomes wider [26] and narrows the envelope width down, giving further aid in alignment.[1]

For the actual measurements, a white LED is used. The broad spectrum is achieved by coating a blue InGaN based LED with phosphor. The blue pump light undergoes phosphorescence and is emitted at a longer wavelength. The LED spectrum then shows a narrow blue peak and a wider peak spanning from green to red, while the LED looks white to the human eye.

The light source spectra were measured with an Ocean Optics USB2000 spectrometer. The two spectra are illustrated in figure 4.10a. The vertical axis in the graph is arbitrary and the maximum values of the two spectra are not to scale. The red LED spectrum shows a roughly gaussian peak centered at 651 nm and with a bandwidth of 27 nm. In the white LED spectrum, the separate narrow blue pump LED peak and the wider phosphorescence peak of longer wavelengths are observed.

When using a white LED in the interferometer setup, the observed fringe pattern depends on the source spectrum combined with the spectral response of the detector. A graph of the color channel spectra of the DFK41 camera can be found in the ICX205AK CCD sensor datasheet. [33] The provided graph shows the combined result of the silicon sensor spectral sensitivity and the RGB color filter transmission curves. The graph is reproduced in figure 4.10b. Numerical values are not provided, so approximate values for the curves were extracted from the electronic PDF version of the data sheet.

[1] Incidentally, white light interferometry was also utilized for this same reason in the famous, previously mentioned Michelson–Morley experiment. Michelson and Morley set up the alignment of their interferometer using coherent yellow light of a sodium flame. For actual measurements, however, white light was used. This is because the measurements were recorded by counting the fringes visually. With monochromatic light, the lack of temperature compensation and various external disturbances like horse traffic made the fringes shift or blur uncontrollably, having the observers lose track of the fringes. Using a white light source provided a fixed reference point for detection and calculation. [25]

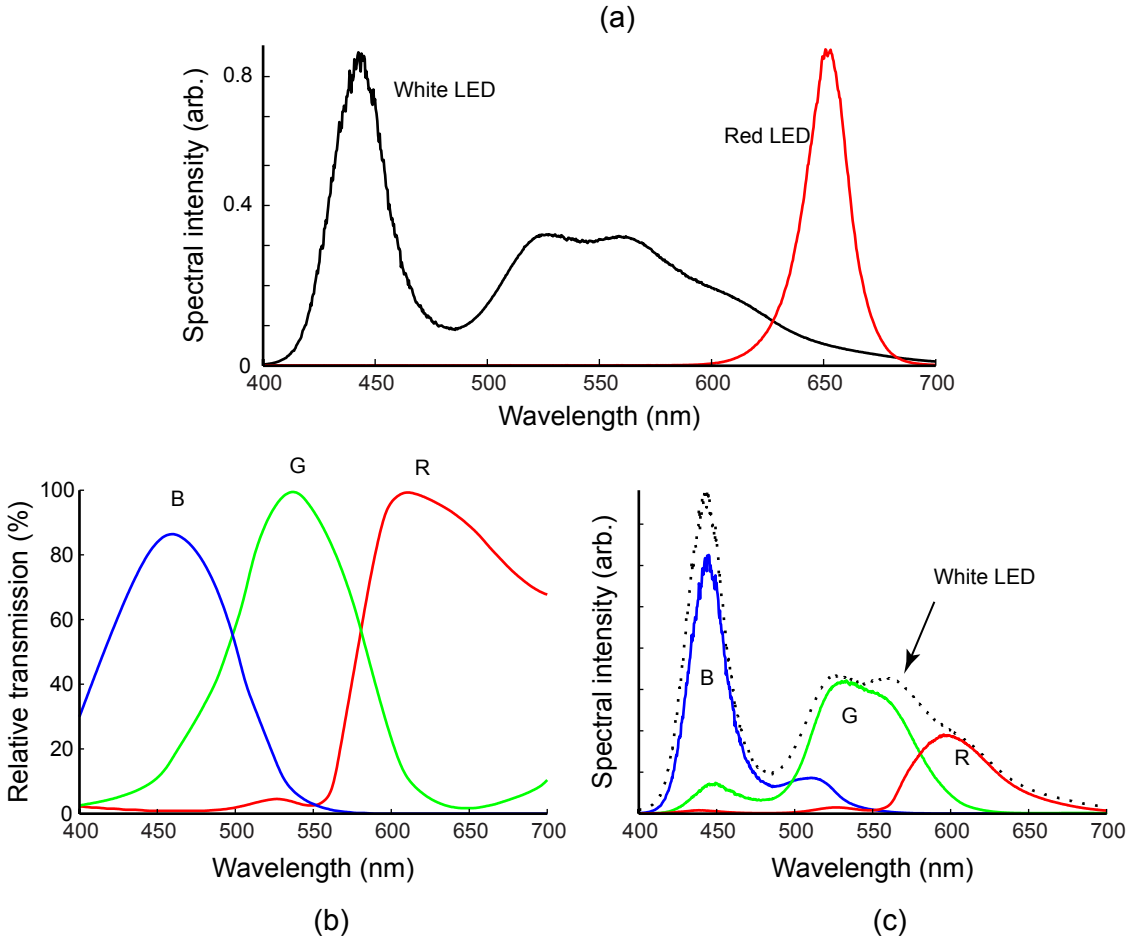

Figure 4.10. **(a)** Measured spectra of the white and red LEDs used as light sources. The spectra are normalized to the same maximum value. **(b)** Sensitivity of the camera sensor, combined with spectral transmission of the RGB color filters used on the Sony ICX205AK sensor Bayer matrix. Extracted from datasheet graphic. [33] **(c)** The effective combined color channel spectra, calculated by weighing the spectral response of each RGB channel with the spectrum of the white LED source.

In figure 4.10c, the measured white LED spectrum is multiplied with the approximate extracted curves for the RGB color channel responses. The original spectrum is shown dashed.

Actual color photographs of interference fringes produced by the two LEDs are presented in figure 4.11. The interference geometry matches the simulation shown in figure 3.8: for maximum contrast, two identical mirrors are used in the sample and reference arms. One of the mirrors is tilted such that the interference fringes show up as a lateral pattern throughout the frame.

The red LED produces a longer coherence length, with decreasing fringe contrast visible only at the corners of the frame. The white LED produces a much narrower area of oscillating intensity. However, in the individual color channels, the fringes are observed on a wider scale due to the narrower spectral bandwidth of a single

channel. In the color photograph the effect is visible as fringes of nearly constant intensity but alternating color outside the area of strongest fringes.

In figure 4.11b, the fringe envelope is seen to be slightly irregular and asymmetric, which results from the two-peaked LED spectrum and dispersion in the imaging system. However, filtering the light with the green color channel filter suppresses the blue peak and makes the resulting interferogram more regular. Also the red and blue color channel filters produce a reasonably clean spectrum. A least-squares fit of a gaussian function to the measured light source spectra, together with actual measured interferograms resulting of different combinations are illustrated in figure 5.1. When using only a single color channel, the green channel should be preferred, since it has a share of every other pixel on the Bayer matrix and therefore produces the best spatial resolution.

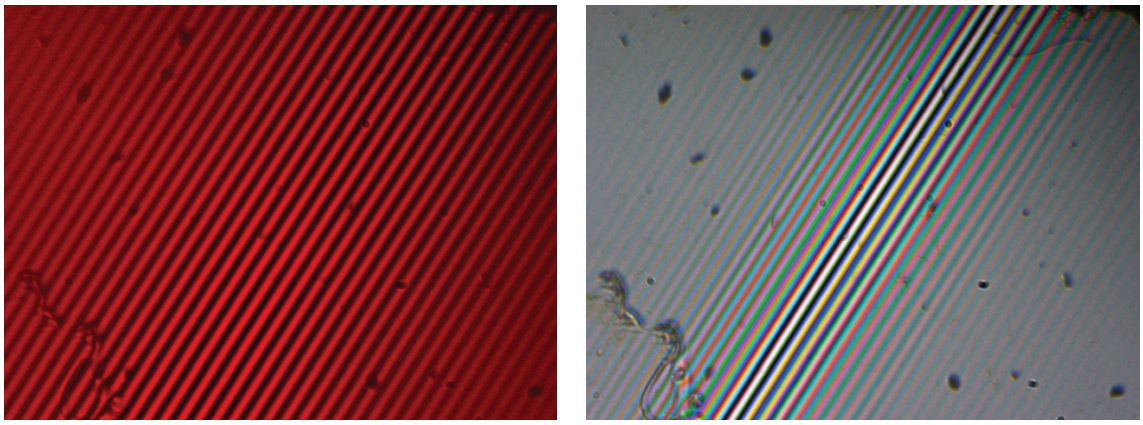

Figure 4.11. Photographs a interfering images of two tilted mirrors, showing the interference fringes and coherence lengths produced using illumination with **(a)** a red LED or **(b)** a white LED. Compare with figure 3.8

4.2.6 Environmental control

Compared to higher frequency ultrasonic devices, the large amplitude vibration in low frequency MEMS devices make them more sensitive to the damping action of air molecules around the vibrating structures. For this reason, they normally exhibit reduced performance in atmospheric pressure. To avert this, in final applications, MEMS resonators are typically hermetically sealed inside a vacuum casing.

For being able to optically probe MEMS vibration during research and development of the devices, a vacuum system designed and implemented in [19] is used. A small vacuum chamber is laid on top of the pad housing the sample under study. On top of the chamber there is a window of optical glass through which probing can be done from outside the vacuum.

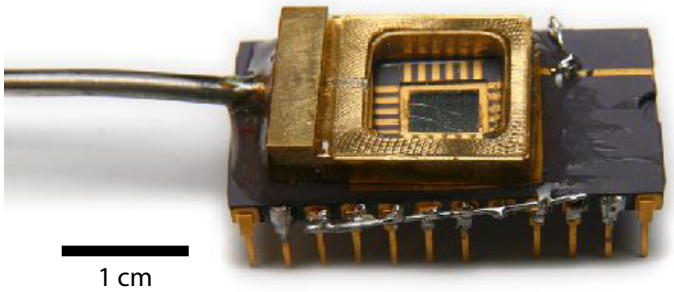

Figure 4.12. A vacuum chamber, used for lowering the air pressure enough not to have an effect on the vibrational characteristics of the MEMS device. Here, a hollow brass casket is glued around the MEMS device which is bonded on an open ceramic dual in-line package (CDIP). On top of the casket, a thin optical glass window is then glued to allow imaging the sample. A vacuum pump is used to pump the air out of the chamber via the tube on the left.

The air is pumped out of the chamber with an Alcatel rotary vane vacuum pump via a short metal tube attached to a silicone hose. Silicone, being a porous material, is not optimal for demanding vacuum applications because of leakage of air through the hose walls and joints. The advantages of using silicone are its low weight and flexibility, which makes it a suitable material for attaching to the vacuum chamber which is translated in relation to the imaging system. With the small total volume of the vacuum chamber, the system readily reaches a sufficient pressure level of 0.1 mbar. At this pressure, the performance of MEMS resonators is typically not pressure limited. [19] [38]

4.2.7 Mechanics

For positioning the sample within the imaging frame and for collimating the interferometric setup, two XYZ translator stages are used. The sample is attached to a small circuit board fastened to a manually operated translator stage. The lateral translation directions X and Y are used to position the region of interest on the sample within the image frame. The translation direction Z is used to move the sample along the optical axis to bring the sample surface in focus.

The reference mirror is attached to a New Focus Picomotor motorized XYZ translation stage. The Picomotor translator features screw thread translation on three axes, and uses two piezoelectric actuators which use friction to rotate the screws by expanding and contracting with high frequency. The motorized translation can also be overridden by turning the screws manually like with a traditional manual translation stage. The motors can be computer controlled to automate measurement

cycles and the shortest translation step is of the order of 30 nm.

Controlling the lateral X and Y positions of the reference mirror is only needed when setting up interference, to be able to translate the mirror edge to be visible in the imaging frame, for determining when the mirror surface is in focus. When carefully focusing both the mirror and the sample surfaces, interference is observed once the optical path lengths become equal.

Both the reference mirror and the sample are attached to mirror mounts which allow precise adjustment of tilt. Inclination of the reflecting surface results in the reflected wavefront being tilted, so the sample and reference mirror are adjusted to be as orthogonal to the beam as possible. A tilted angle between the interfering wavefronts results in interference observed as a lateral fringe pattern (figure 3.4b). When reaching focus for the first time the tilt mismatch is typically very large. When using a light source of narrow bandwidth, the pattern of lateral fringes fill the entire image frame. With wider spectrum illumination like a white LED, interference is observed as a narrow line.

By carefully adjusting the tilt, the fringes become wider and ultimately, when the tilt of both wavefronts match, interference is observed as the whole image darkening and brightening when moving either surface in the Z-direction. This happens also without both wavefronts being perfectly orthogonal, if they are tilted by the same amount. Too much tilt results in parts of the sample falling outside the focal depth of field of the optical system, such that at the edges of the imaging area sample features are out of focus. Additionally, too much tilt will make the distribution of reflected light shift outside the imaging sensor.

Currently, the computer controlled translation is done in the reference arm with the Newport New Focus Picomotor stage. Using the reference mirror for scanning has a drawback of limiting the available range for surface profile measurements to the length of the depth of field (DOF) of the optical system, i.e., the range of depths at which an object appears to be in focus. Translating the reference mirror far enough to fall out of focus means that interference can be detected only when also the sample is out of focus by the same distance. A defocused image degrades spatial resolution and the quality of interference.

Carrying out the translation in the sample arm, however, would keep the reference mirror surface always sharply in focus and would make sure that interference is observed only when the sample surface is in focus too. This limits the range of profile measurements only by the motion range of the translator stage. The vertical range of the devices of interest is typically at most a few micrometers. With the low power optics and high focal ratio of the current imaging optics, this range is well within the depth of field.

The camera, optics and translators are assembled in an aluminium rig, which is fastened onto a stabilized optical table.

4.3 Software

For PC automation of the measurement setup, an instrument control software was developed with the National Instruments LabVIEW visual programming language. LabVIEW was chosen as the platform because of its ease in creating graphical user interfaces, facilitation of rapid program development and the availability of interfaces for controlling instruments such as the signal generators, the camera and the motorized translation stage.

4.3.1 LabVIEW programming

LabVIEW (*Laboratory Virtual Instrument Engineering Workbench*) is designed as a platform for producing software with user interfaces and functionality that closely resemble those of physical scientific instruments found in a laboratory environment. Hence, an application developed within LabVIEW is called a Virtual Instrument (VI).

A LabVIEW VI consists of two main parts, a front panel and a block diagram. The front panel acts as the graphical user interface of the program and houses different controllers and indicators such as numeric text fields, buttons, switches, graphs, etc. In the block diagram, the front panel objects act as sources and sinks of data. The data is controlled in a flow chart type fashion, with a range of available building blocks that correspond to various data operations, functions and program flow controls familiar from traditional text based procedural programming languages. Repeating program structures can be encapsulated into sub-VI's for reusability and keeping the block diagram readable.

As such, the execution order of various structures in the block diagram is not predetermined, but follows a data flow execution model. [39] Any calculation or other higher level operation in LabVIEW is represented as a block diagram object with input and output terminals. An object executes when all obligatory data at its input terminals is available. Once the execution is finished, the object outputs data from its output terminals. For example, the summation function takes two numbers wired at its input terminals and outputs their sum to the single output terminal. Because of this ambivalence of execution order, the software has to be designed such that data flow will govern the execution of different parts of the code.

An example of a part of the block diagram of the developed control software is illustrated in figure 4.13.

4.3.2 Hardware control

Different hardware to be interfaced with the software are the camera for collecting image frames, the two signal generators for driving the vibration and synchronized

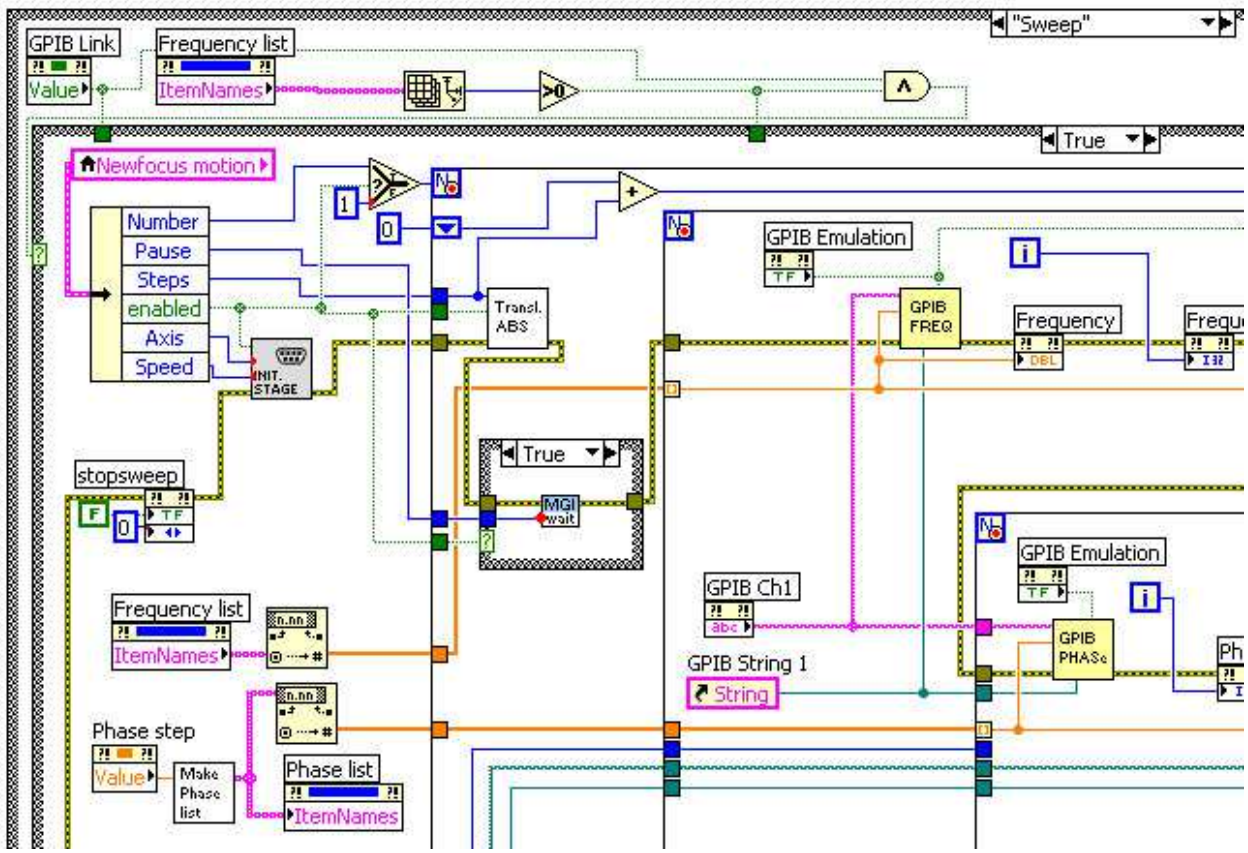

Figure 4.13. Example of the block diagram -based visual programming style of LabVIEW.

stroboscopic illumination of the sample and the translation stage for altering the optical path difference needed to record image samples over the span of the coherence length.

The Imaging Source, the manufacturer of the DFK41 CCD camera used in the setup provides a LabVIEW interface for controlling the camera. The interface consists of a set of VI's (LabVIEW building blocks) that wrap around the functionality of the generic *IC Imaging Control* development library used to control imaging products by The Imaging Source. The camera is interfaced over USB.

The Newport New Focus Picomotor XYZ translation stage is controlled through a Intelligent Picomotor Control Module connected to the computer via a RS-232 serial port. In the command protocol, a motor is selected and then translated either backward or forward for a given number of steps with a given frequency (speed).

The Hewlett Packard and Agilent signal generators are connected via GPIB (*General purpose interface bus*) with an PCI GPIB interface card. Support for GPIB communication, a de facto industry standard since the 1970's, is an integral part of the LabVIEW system, with several tools for device control and data acquisition. The *GPIB Write* function is used to send simple text based commands for controlling

the waveform, frequency and pulse lengths of the two signal generators. [40]

4.3.3 User interface

The graphical user interface (GUI) is designed to show all necessary controls and indicators for using the software at once on the front panel. While intuitiveness is not an important premise of the design, certain usability improvements are implemented. In any case, the user is expected to have extensive knowledge of the operation of the stroboscopic interferometer setup.

A screen shot of the GUI is shown in figure 4.14.

Camera settings

The majority of the screen area is taken up by the camera view, which shows the live image from the connected camera.

The right hand side camera settings panel shows a list of available cameras connected to the computer. After opening a connection to a camera, different imaging settings can be chosen. When using a one shot color camera, the video format selection specifies which color interpolation scheme is used for the Bayer color matrix image:

BY8 Raw B&W frames transferred over USB. Debayering done on computer. Results in 3×8 bpp color images.

Y800 Raw B&W frames transferred over USB. No debayering applied. Results in 8 bpp B&W images.

YUY2 Debayering done on camera. Color frames transferred over USB. Results in 3×8 bpp color images. Due to the larger amount of data, does not support the highest frame rate of 15 fps.

The camera exposure time and sensor gain value can be adjusted with sliders. Automatic control of exposure or gain can be selected through checkboxes. Automatic exposure control is convenient for rough framing and focusing. The actual measurement data, however, has to be recorded with constant, preselected exposure values such that the resulting pixel intensities will be consistent.

The zoom setting of the camera view can be altered with a slider and three quick buttons. The 1280×960 pixel image is fully shown in the view using a 50% zoom setting. The highest magnification of 500% is useful for fine focus control.

Generator options

Controls for the signal generator parameters are found on the upper left hand side. Waveforms are fixed as sine (SIN) and pulse (PULS) for the sample and the illumi-

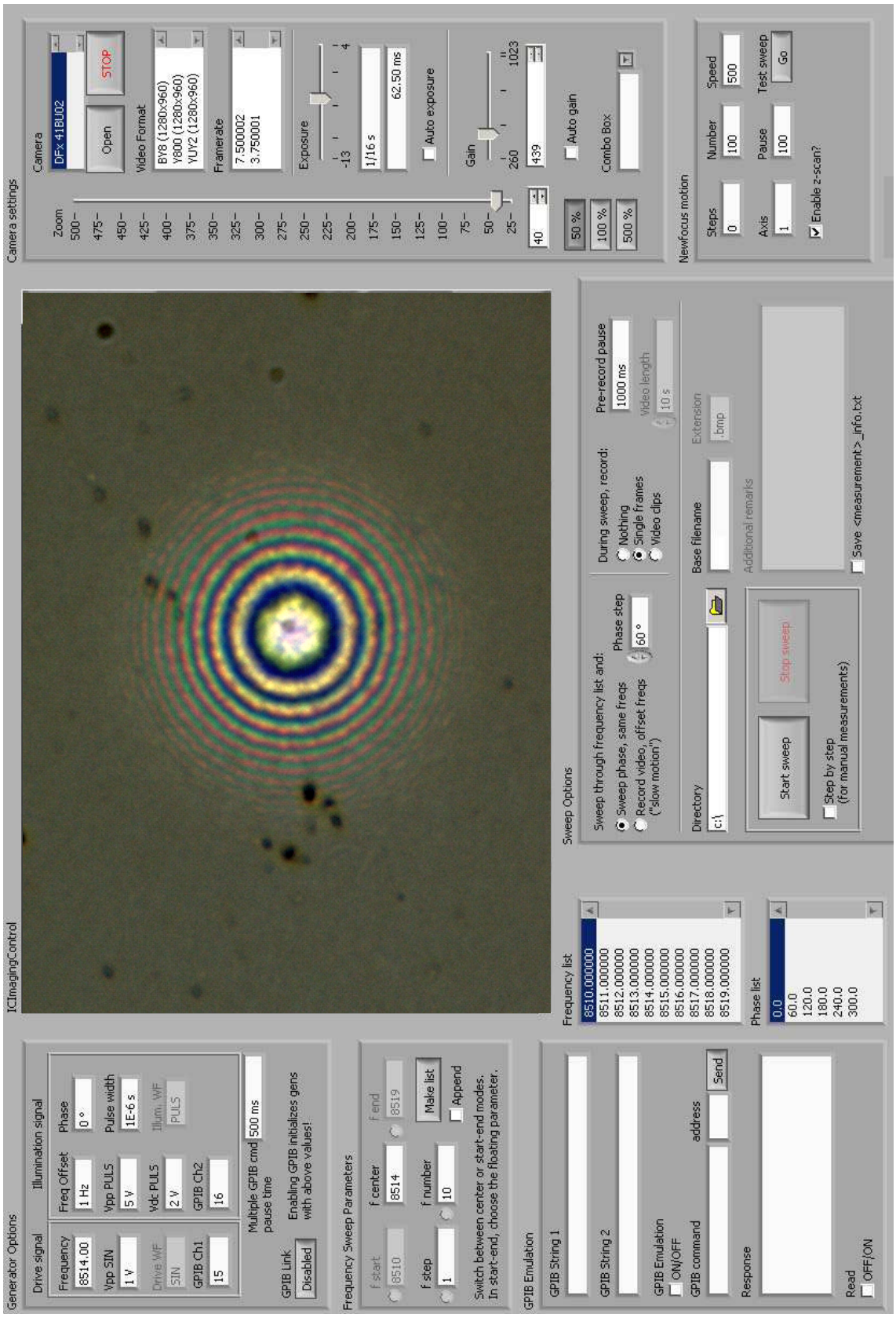

Figure 4.14. Graphical user interface of the control software.

nation signals, respectively. The voltage levels of the generator outputs are chosen according to the requirements of the sample under study and the LED driving electronics used. The resulting duty cycle (percentage of time the LED is switched on) is given by

$$D = f \cdot t_p, \tag{4.1}$$

where f is the frequency and t_p the pulse width.

Typical duty cycle values range from under 1% up to around 5%. Because the LED stays on for only such a small fraction of time, it can be used with a smaller resistor and therefore much higher temporary current than when normally connected to a 12 volt DC circuit. Because of this, care has to be taken by the user not to enter a too high duty cycle that might destroy the LED.

The desired frequency is set for the sample drive generator. The frequency of the stroboscopic illumination is set as an offset to the sample frequency. Using a 1 Hz offset between the frequencies makes the sample vibration appear to be slowed down to a 1 Hz periodic motion in the camera view. Using a zero offset will apparently freeze the vibration in place. The phase difference of the signals can then be altered and used to examine the vibrating sample at different phases during the vibration period.

For setting the phase difference of the pulsed signal in relation to the sine signal, a separate GPIB command has to be issued. [40] To ensure that consecutive commands do not interfere with each other, a small delay between the commands can be specified. A vast automated measurement run, however, can include thousands of commands sent to the signal generator, so the delay should be kept as short as possible for preventing a cumulative delay of several hours during the whole measurement.

Changing any value on the Generator Options panel results in the new value immediately being updated to the generator. This enables cycling through different values on the fly using the arrow keys, e.g., when manually searching the resonance frequency. If required, the GPIB link can be disabled when entering new values. Enabling the link again initializes the generators with all of the values of the Generator Options panel.

Furthermore, the GPIB emulation option can be enabled in the lower left hand side panel when required. In the emulation mode GPIB commands are written to the *GPIB String* text controls rather than sent to the generators. Inside the panel it is also possible to send raw GPIB commands to the generators or any other connected device with a GPIB address. The devices response can also be queried and displayed in the text box.

Frequency sweep parameters

The frequency sweep parameters panel is used for generating a frequency list for the automated measurement run to cycle through. Two different modes for generating a list are available. In the center mode, a central frequency, number of frequencies and the desired separation between frequencies are entered. A list of frequencies is then generated symmetrically around the central frequency.

In the start-end mode, both starting and ending frequencies are specified. A list of frequencies between them is generated based on either the number of points or the specified frequency step. One of the four parameters is floating and will automatically be calculated based on the other three. The floating parameter is selected with a radio button. When specifying a frequency interval that is not divisible by the given step, the end frequency will automatically also be a floating parameter.

Switching between the center and the start-end modes is done automatically when clicking any of the disabled fields, which also updated their values when entering frequency parameters in the other mode.

When the frequency list is generated and GPIB link is enabled, clicking an element in the list will change the frequencies of the generators automatically.

Optical sweep options

The New Focus motion panel on the lower right provides commands to translate the reference mirror with the motorized XYZ stage. The selected axis can be translated by a burst of translation steps with a specified length and frequency. A specified amount of these bursts can be done with a chosen time interval.

The Test sweep button triggers the motion with the given parameters and can be used for manually translating the sample. The *Enable z-scan* checkbox can be left unchecked to skip the stage translation loop for, e.g., in plane vibration measurements.

Recording options

For conducting an actual automated measurement run, various options are available in the lower middle Sweep Options panel. During a measurement run, the generated list of frequencies is iterated through. When iterating over each frequency, sweeping over the different phases of the vibration cycle can be done in two ways.

The first option is to set equal frequencies for both generators and iterate over sequential phase difference values. A single frame is captured with the camera with every frequency and phase value.

Entering the phase step value automatically generates the phase list below the frequency list. Similarly to the frequency list, selecting any element in the phase list will update the selected phase value to the pulse generator whenever the GPIB link is enabled.

The other option is to set offset frequencies for the generators and record a slow motion video for each frequency in the list. In this option the offset value is read from the Generator Options panel.

A video clip of the apparently stationary sample can also be recorded when using the phase sweep option. However, the still frame option is disabled when using the offset frequency option, since imaging single frames of the slowly moving subject would be needless.

For recording interferograms to obtain three-dimensional data, the measurement cycle has to be extended to sweep through different optical path length difference values by moving the reference mirror with the translation stage. For reproducible positions between different frequency values, the z-translation is implemented as the outermost loop, i.e., every translation step is executed only once and all of the frequency and phase values will be swept through before taking the next translation step. The translation sweep is only executed when the Enable z-scan checkbox in the translation options panel is checked.

Finally, the directory and naming of recorded image or video files can be configured. Each translation, frequency and phase value is appended to the base of the file name. Additionally any remarks concerning the measurement can be entered. The remarks will be written to a log file together with all of the configuration values on the front panel.

For testing other imaging hardware than those supported by the software, the user can enable the step by step option. Here the user is presented with a message dialog every time the camera should be triggered manually. The measurement cycle is only continued once the dialog box is dismissed.

Chapter 5

Data and post processing

The data produced by the measurement setup consists of 1280x960 pixel images of raw grayscale values. For obtaining information of the vibration characteristics of measured samples, the data is post processed as follows.

Through the cross-section of a sequence of images, the green channel intensity values recorded by a single pixel are examined to observe the interferogram pattern. The modulation envelope is extracted from the fringe pattern data. From the envelope, its central location is determined, which then gives the surface elevation at the considered pixel. The elevation is determined for every pixel throughout the image, which yields a three-dimensional surface measurement of the sample.

The acquired stationary surface shape represents a single phase value of the vibration cycle. The processing is repeated for other image sequences acquired with different phase difference values between illumination and vibration. After this, a set of three-dimensional measurements have been constructed throughout the vibration cycle. Vibration amplitude and phase can now be calculated for mapping the vibration across the imaged area. The collection of surface profile measurements can also be used for constructing a three-dimensional animation of the vibrating surface.

Usually, this process is then repeated across a range of frequencies, which typically span around a resonance frequency. By looking at the vibration amplitude at a location on the surface, the frequency response curve (vibration amplitude against frequency) can be plotted.

A full measurement cycle with a long axial sweep, many frequencies and dense phase sampling produces massive amounts of data. For example, scanning through 500 z-steps for 20 frequencies with a 10° phase resolution (36 phase steps) produces 360000 images, with a total of over 400 billion pixel values. Storing them at 8 bits per pixel takes up 400 gigabytes of hard disk space when using an uncompressed bitmap format.

5.1 Measured interferograms

The shape and quality of observed interferograms is crucial for determining the location of the envelope function. [41] In the current setup, five different kind of interferograms can be produced by light source and color channel combinations: a red LED, a white LED in any of three color channels or as gray scale average of all channels. The red LED is always used with the red channel.

The measured light source spectrum (figure 4.10) can be used to calculate the shape of the expected interferogram. The interferometer output signal is the real part of the discrete fourier transform of the source spectrum. [42] Equivalently, the signal can be simulated simply by calculating a sum of cosine functions [43] with their wavelengths and amplitudes determined from the measured spectrum data:

$$I(z) = \sum_{k=1}^{N} S\left(\lambda_k\right) \cos\left(2 \cdot \frac{2\pi}{\lambda_k} \cdot z\right), \tag{5.1}$$

where z is the axial displacement coordinate, λ_k an individual wavelength in the spectral data and $S(\lambda_k)$ its corresponding spectral intensity.

Actual fringe patterns produced by different light source and color channel combinations were measured by averaging a 100x100 pixel area from an image sequence of a smooth aluminium surface deposited on a quartz substrate, altering the optical path difference by approximately 30 nm between every image.

The measured fringe patterns agree well with calculations, as seen in figure 5.1. The width of the simulated interferogram matches measured patterns with all five spectrum combinations. A least-squares gaussian fit is also shown for each spectrum. The red LED is the closest approximation of a gaussian source and it is observed to produce the cleanest fringe pattern. It also produces the widest interferogram because of having the narrowest spectral bandwidth of about 30 nm.

The white LED combined with individual color channel filters produce approximately gaussian spectra with minor side lobes, which result in reasonably clean fringe patterns. The slight asymmetry observed in the measured fringe patterns, especially in the green and blue color channels, results from dispersion in the optical system. [43] In a system without dispersion, any spectrum would result in a symmetric fringe pattern. [27]

The total spectrum of the white LED is distinctly two-peaked, which produces a distorted fringe pattern in both the measured and simulated data.

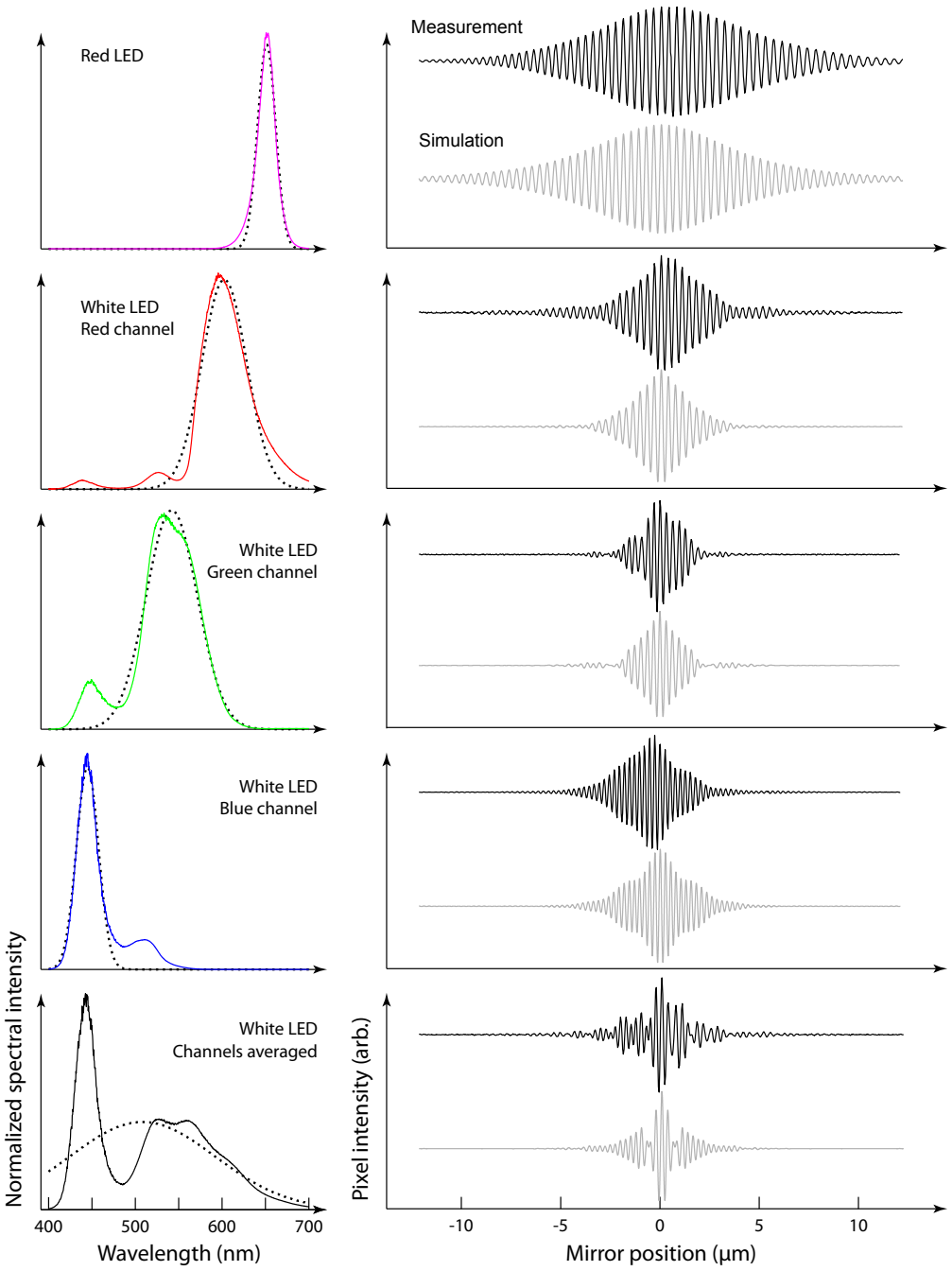

Figure 5.1. Spectra of different light source and color channel combinations, presented together with both calculated and measured interferograms produced by them. **Left column:** Measured spectra of light sources. Red and white LED sources were used. White light was analyzed in the three individual color channels and as averaged gray scale values. Dashed curves are least squares fits of gaussian functions to the spectrum data. **Right column:** Measured interferograms (black) compared to simulations (gray) calculated from the spectrum.

5.2 Extracting envelopes

When an interferogram signal is recorded in a single pixel, finding the surface height at that pixel involves finding the location of strongest oscillation amplitude within the fringe pattern, i.e., finding the location of the maximum value of its envelope function. Good quality, low noise data and sophisticated signal processing techniques enable sub-nanometer resolution in extracting surface profiles from measured interferograms. [44] [45]

The general form of the observed intensity in a white light interferometer is [46]

$$I(x,y,z) = a(x,y) + b(x,y)\gamma\left(z - 2h(x,y)\right) \times \cos\left(4\pi/\lambda_0 \cdot (z - 2h(x,y)) - \alpha(x,y)\right). \tag{5.2}$$

Here, (x, y) is the pixel location on the transverse image plane and z is the position of surface of the object along the optical axis. $a(x, y)$ and $b(x, y)$ are offset and gain type quantities that are related to the reference and measurement light beam intensities. γ is a non-negative function describing the fringe envelope, with an argument of zero corresponding to the envelope peak. Thus, on the z-axis, the envelope peak that is of interest is located at $z = 2h(x, y)$, where $h(x, y)$ is the surface height at the given point. Again, the factor 2 comes from the round-trip geometry in the Michelson interferometer. A phase change on reflection that is due to the complex reflectance of the surface determines the parameter α. Typically α is small and assumed to be zero but this is generally not the case. α varies with the dielectric properties of the surface. [27]

Processing white light interferometry data involves measuring $I(x, y, z)$, extracting $\gamma\left(z - 2h(x, y)\right)$ and locating its maximum to find $h(x, y)$. Notice that both γ and the cosine term depend on $z - 2h$, which means that in ideal conditions, the fringes move with the envelope, i.e., the fringe pattern below the envelope doesn't change shape, given α stays constant. This detail offers crucial help in locating the envelope peak, but is often overlooked in literature.

Extracting the envelope function can be done in various ways, most of which exploit the fact that I is a product of a low-frequency envelope signal and a high frequency cosine carrier signal. The advantage here is that in almost every typical application, the two are non-overlapping in frequency space.

Therefore, by calculating a Fourier transform, the cosine carrier signal can be filtered out in the frequency space to yield only the envelope function γ. [47] Other methods to directly find the envelope center via the frequency space also exist. On the downside, these algorithms are very intensive computationally. Easier and more efficient solutions are based on the Hilbert transform.

The usefulness of the Hilbert transform in envelope extraction is due to *Bedrosian's theorem*. The theorem deals with functions that are products of low- and high-frequency components with non-overlapping spectra, like the typical white light

interferogram. According to Bedrosian [48], the Hilbert transform of such a function is equal to the low frequency function multiplied by the Hilbert transform of the high frequency function, or

$$H\{f_L \cdot f_H\} = f_L \cdot H\{f_H\}, \tag{5.3}$$

where $H\{f\}$, f_L and f_H are the Hilbert transform, the low-frequency function and the high-frequency function, respectively. The Hilbert transform of a cosine function is the sine function, so for a modulated signal

$$J(z) = \gamma(z)\cos(\omega z + \phi), \tag{5.4}$$

$$\begin{aligned} H\{J(z)\} &= H\{\gamma(z)\cos(\omega z + \phi)\} \\ &= \gamma(z) H\{\cos(\omega z + \phi)\} \\ &= \gamma(z)\sin(\omega z + \phi), \end{aligned} \tag{5.5}$$

which means the Hilbert transform performs a 90° phase change from cosine to sine on a modulated oscillating signal.

Now let us define

$$G(f(z)) = f(z) + iH\{f(z)\}, \tag{5.6}$$

a complex valued signal with the original signal $f(z)$ in the real part and its Hilbert transform in the imaginary part. For our modulated signal $J(z)$ (equation (5.4)),

$$\begin{aligned} G(J(z)) &= J(z) + iH\{J(z)\} \\ &= \gamma(z)\cos(\omega z + \phi) + i\left[\gamma(z)\sin(\omega z + \phi)\right] \\ &= \gamma(z)\left[\cos(\omega z + \phi) + i\sin(\omega z + \phi)\right] \\ &= \gamma(z) e^{i(\omega z + \phi)} \end{aligned} \tag{5.7}$$

The modulation envelope of our signal can now simply be calculated by as the absolute value of the complex G:

$$\gamma(z) = |G(J(z))|. \tag{5.8}$$

Furthermore, the complex argument (polar angle) of G contains information about the phase of the carrier signal of J, i.e., of the fringes. In MATLAB and some other data analysis environments, the combined complex signal can be calculated simply with the function `hilbert`, which returns the combined complex signal. The steps of extracting the envelope with the Hilbert transform are illustrated in figure 5.2.

Using the Hilbert transform for envelope extraction is straightforward and gives near-perfect results for typical interferograms. [49] When computational efficiency is a limiting factor, like when seeking real time envelope detection, faster approximations to the Hilbert transform can be used. The 90° phase shift by the Hilbert transform applies over a wide band of frequencies, but it is only needed over the

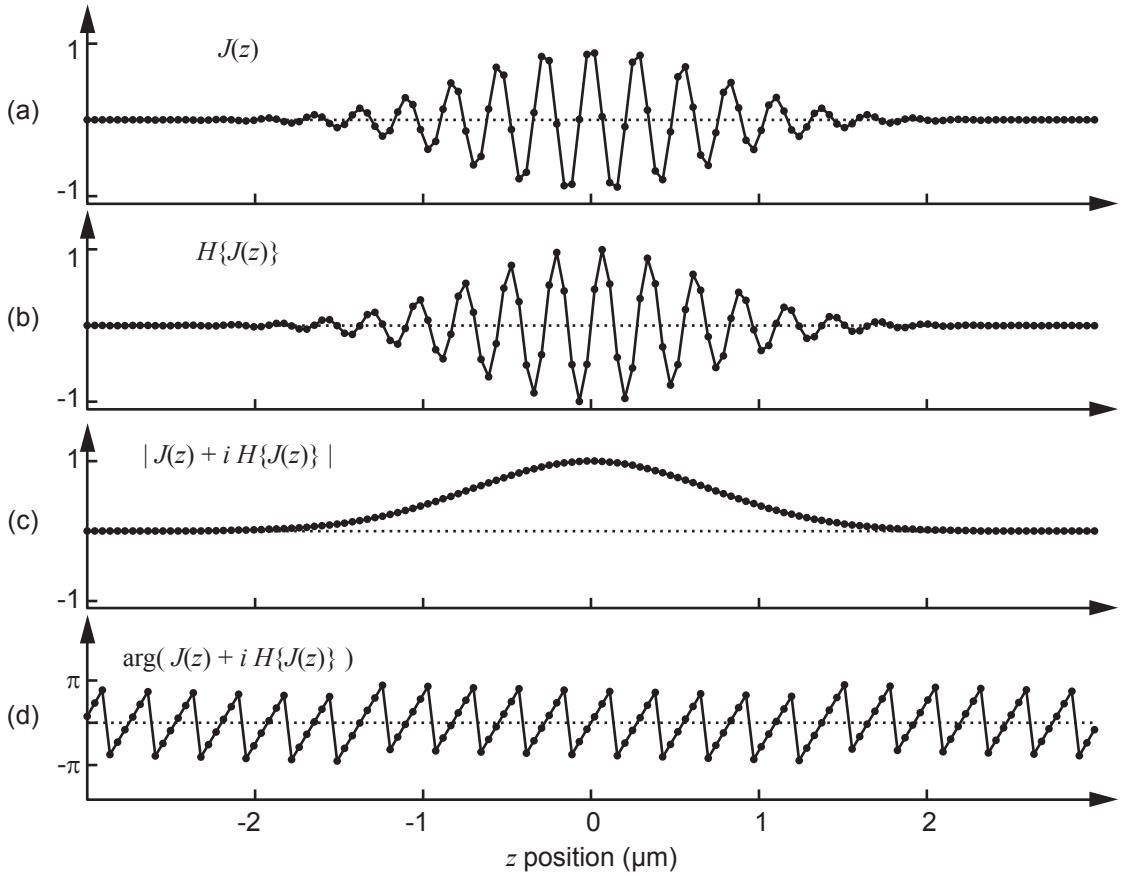

Figure 5.2. Using the Hilbert transform to analyze the interferogram. **(a)** The original signal, depicted here by an ideal, noiseless cosine function with a gaussian modulation, centered at $z = 0$. **(b)** The signal's Hilbert transform. Note the fringes shifting to the right by 90°. **(c)** The absolute value of the combined complex signal yields the modulation envelope. **(d)** The argument or phase angle of the modulated signal. Note the clean sawtooth pattern of the linearly increasing phase value, shifted back to $(-\pi, \pi)$.

narrow frequency band of the oscillating carrier signal. Various approximations and their suitability has been researched in [46]. Probably the most popular example is the five-point finite impulse filter algorithm where the square of the carrier modulation envelope is found by the expression

$$M^2 \propto (I_2 - I_4)^2 - (I_1 - I_3)(I_3 - I_5), \tag{5.9}$$

Where I_k are five consecutive samples from the interferogram. M then gives the modulation strength at the location of I_3. This modulation value can then be calculated by going through the sampled interferogram, to obtain the complete extracted envelope (γ). Discrete approximations like this are sensitive to the size of the sampling step and work best when sampling with a 90° phase interval. [46]

The next step is to find the central location of the envelope peak. A simple and

fast approach is just to select the z value corresponding to the maximum value of $\gamma(z)$. Obviously, the resolution of this method is limited to sampling interval of the data, i.e., it is not suitable for sub-pixel peak location estimates. Secondly, even slight amount of noise present in the interferogram can make the neighboring sample locations be chosen as the peak value. Therefore the location of maximum value is used only as a starting point for improving the estimate.

With the rough estimate of the envelope peak location, $2N + 1$ values around it are selected for curve fitting. The goal is to fit a suitable, symmetrical curve to the data and obtain the central position from the parameters of the best fit. For a gaussian function, the least squares fitting method can be carried out. Finding the center of a gaussian peak can also be done by a simplification based on the property that $\log(e^{-z^2}) = -z^2$, i.e., the logarithm of a data set containing a gaussian peak will show a parabolic peak. The fitting of a parabola can be done via polynomial regression analysis and is more efficient than the general least squares method. As is known, the peak of a parabola

$$q(z) = p_1 z^2 + p_2 z + p3 \tag{5.10}$$

is then found at

$$z_0 = \frac{-p_2}{2p_1}. \tag{5.11}$$

The logarithmic polynomial fit method requires that all data points are well above the noise floor of the envelope data. In most cases, similar results can be achieved by fitting the inverted parabola directly to a narrow region around the peak, without computing the logarithm.

Using the parabolic peak estimation, the envelope center can be acquired with a resolution below one sampling step. For a simulated noise free interferogram, the parabolic peak determination produces nearly perfect results when compared to the known peak location of the simulation. A slight amount of noise will however significantly decrease the accuracy of the estimation.

This problem is overcome by considering the phase data acquired with the Hilbert transform (5.7), shown in figure 5.2d. As seen in (5.2), when the envelope moves along the z-axis, which corresponds to a changing sample surface distance, the fringes and phase values move along as being fixed to the envelope. Furthermore, actual measured phase values are typically quite noise resistant and produce a clean saw-tooth pattern even from noisy interferograms. Therefore the phase values can be used to accurately find the locations of peak values of individual fringes, which are directly related to the surface shape.

Identifying the phase sawtooth of the centermost fringe (using, e.g., the location of the maximum value of the Hilbert magnitude) and estimating the z-value at which phase crosses zero provides a very accurate estimate of the location of the central fringe. Because the phase data is periodic and shifted back between $-\pi$ and π, there is a again the danger of 2π ambiguity if the initial peak center estimate fails to point

the central fringe with the required accuracy of the width of one fringe. The impact and solutions are discussed in the following chapter.

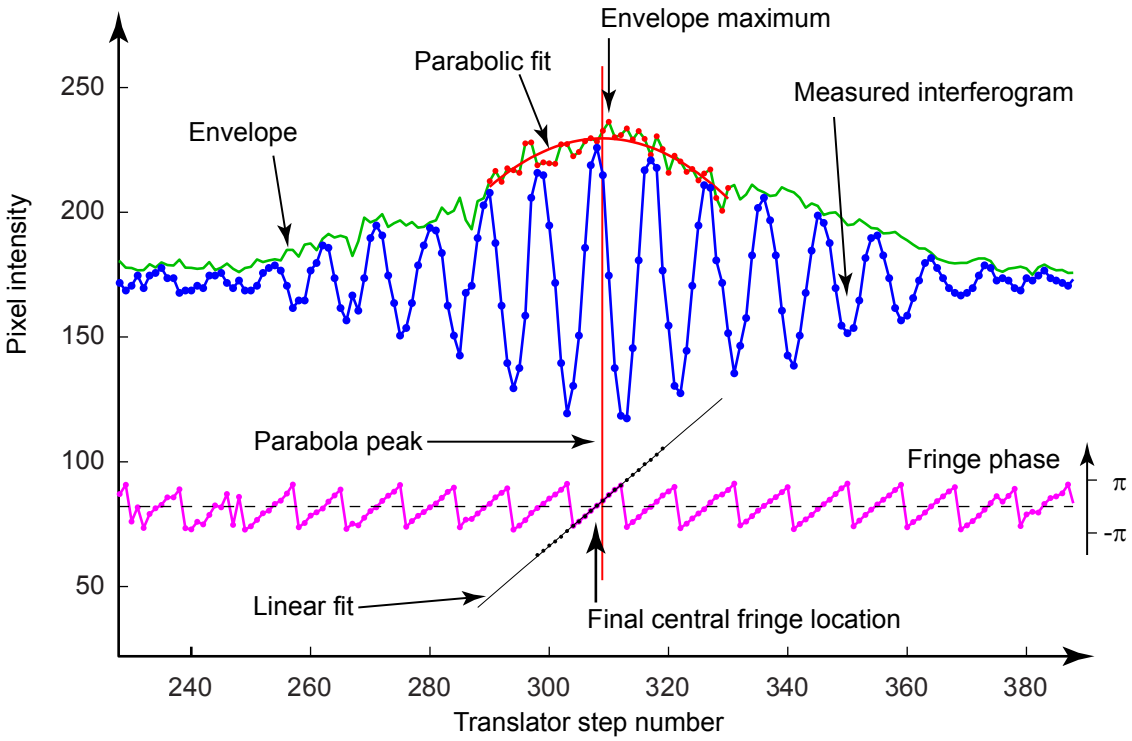

Figure 5.3. Finding the surface position from interferogram data. Measured interferogram from a single pixel using a white LED and the green color channel. From the measured data (blue), the envelope (green) and phase (magenta) of the fringes are calculated. The maximum value of the envelope is located, but it is very susceptible to noise. Therefore, a number of envelope values are selected symmetrically around the maximum value and used for calculating a parabolic fit (red). The peak of the fitted parabola indicates which phase sawtooth to choose for finding the central fringe. A linear fit to the unwrapped phase data is used to find the location of zero phase, which indicates the peak of the central fringe.

The process of locating the envelope center is illustrated in figure 5.3, which shows an actual measured interferogram from a single green channel pixel using the white LED illumination. After calculating the envelope and estimating its peak location with a parabolic fit, a number of phase values are selected around the estimated location. These values are unwrapped for a linear fit, which is then used to accurately determine the location of zero phase. This point corresponds to the maximum value of the centermost fringe of the cosine pattern.

Note that determining the point of zero phase corresponds to a situation where the the peak of the fringe coincides with the center of the envelope. This is true ideally, but not when $\alpha(x, y)$ in (5.2) is non-zero. However, for a uniform surface material, the phase change on reflection stays constant throughout the frame and the difference between the envelope center and the brightest fringe peak stays constant. Therefore,

looking for the zero phase value produces consistent surface profile measurements. If $\alpha(x, y)$ is known, the easiest way of correcting the analysis for it is to multiply the complex Hilbert combination signal (5.7) by $e^{i\alpha(x,y)}$, which will shift the fringes in both real and complex parts by α.

5.3 Stationary surface profiles

The measured data of a single, stationary surface profile consists of a set of two-dimensional images. For every pixel in the images, an interferogram with a number of samples equal to the number of images is acquired. By going through the envelope locating process described above for each pixel yields the surface profile matrix $h(x, y)$, which is essentially a two-dimensional image with a pixel value corresponding to the surface position at that point.

Any tilt mismatch between the sample surface and reference mirror results in skew in the measurement profile. Electroacoustic devices usually contain large planar areas, which makes it straightforward to correct the tilt in the measurements. A planar function is fitted to the reference area with the least squares method and subtracted from the entire measured area.

The calculated data can then be used for producing a three-dimensional surface plot. An example profile is presented in figure 5.4.

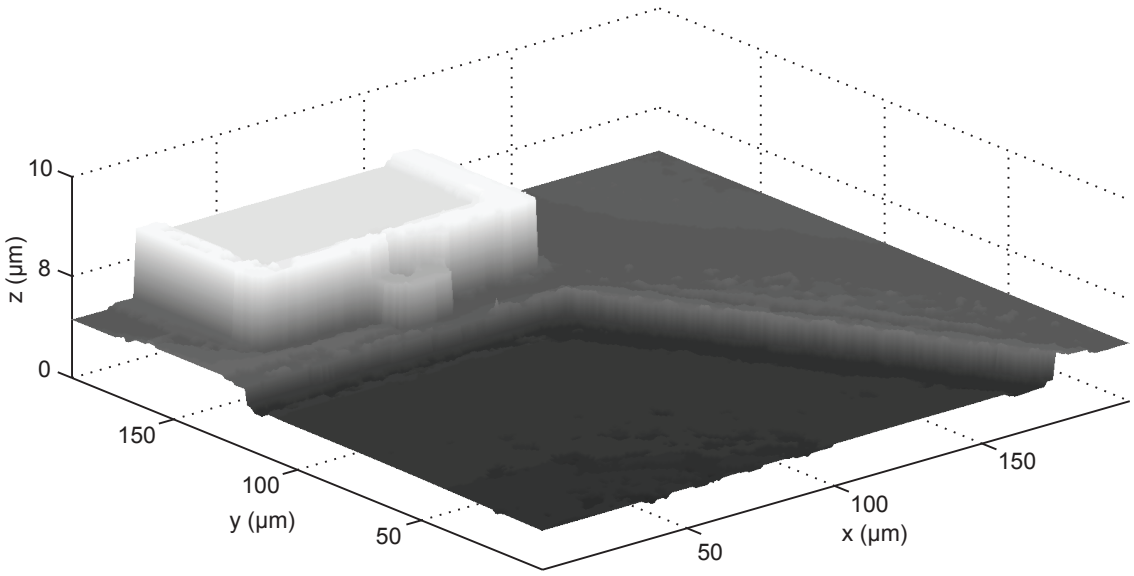

Figure 5.4. Reconstruction of a three-dimensional surface profile measured with the interferometer setup. The measured area is a 200 × 200 µm region of the surface of a MEMS device. The scale of the vertical z-axis is increased by a factor of 5 for illustrative purposes.

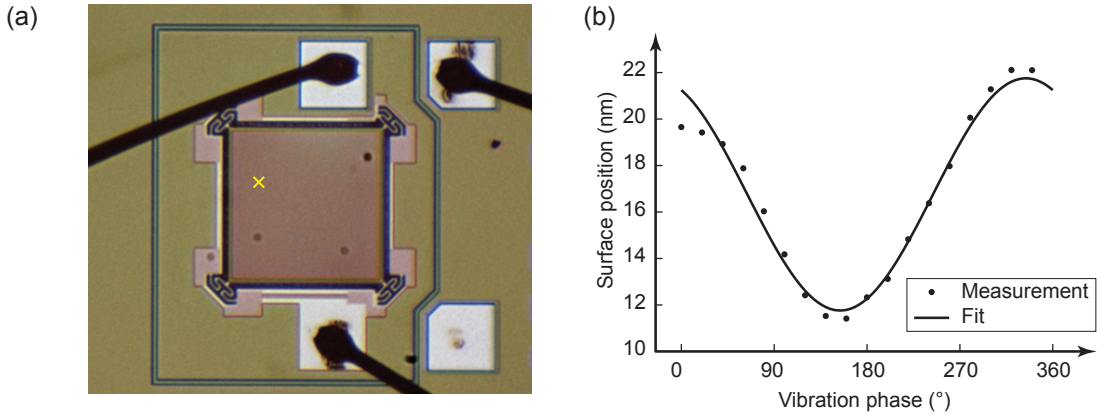

Figure 5.5. Vibration measurements of a MEMS resonator. **(a)** Microscope image of the sample. The resonating structure is the square plate between the bond wires. The length of the square side is 300 µm. **(b)** Surface position at a single pixel, marked with a cross, throughout the measured phase values. A sine curve is fitted by using the Fourier transform. Vibration amplitude and phase at the pixel location are found from the fit parameters.

5.4 Vibration analysis

Data sets for measurements of vibrating samples essentially consist of multiple stationary data sets, with an added fourth dimension of a changing phase difference between the control signals for the sample excitation and illumination pulsing. Since the amount of data collected even for a stationary surface profile is very large, the desire for fine phase resolution will rapidly increase the storage space demand.

For each phase value, the data is processed like described above and a two-dimensional array of surface position values is acquired. The data can then be visualized by a three-dimensional surface plot. Together, the surface plots for each phase offset value can be used to compose an animation of the periodic vibration of the surface.

As a sample for vibration measurement experiments, a piezoelectrically transduced square plate MEMS resonator [50] was used. An out of plane vibration mode at a frequency of 3.1926 MHz is examined. Very satisfactory results were obtained, even considering that 3 MHz is near the upper performance limit of the stroboscopic illumination system of the interferometric setup. A led pulse of 40 ns produces a duty cycle of approximately 1:8. A phase interval of 20° was used to record stationary three-dimensional surface profiles for 18 phase values.

After compiling the set of surface profiles for the different phase values, the surface position value at a single pixel can be examined. At every pixel, a graph of position against phase offset will show a sine curve representing one period of the vibration. From this curve, vibration amplitude and relative phase can be determined by fitting a sine function to the acquired points.

The amplitude and phase of the curve can also be determined easily by calculating a fourier transform of the data. Since the data spans exactly one period of vibration, its amplitude and phase are found, by definition, directly as the absolute value and argument angle of the complex value of the second pixel in the discrete fourier transform.

The calculation of amplitude and phase of vibration is then carried out for every pixel in the image. The measured amplitude and phase maps of the measured MEMS resonator are illustrated in figure 5.6. The resonance mode shows vibration perpendicular to the sample surface. The center and corners of the resonator plate vibrate at opposite phases. An annular zero amplitude nodal line is observed around the center of the plate. The amplitude of the vibration is about 15 nanometers at the center.

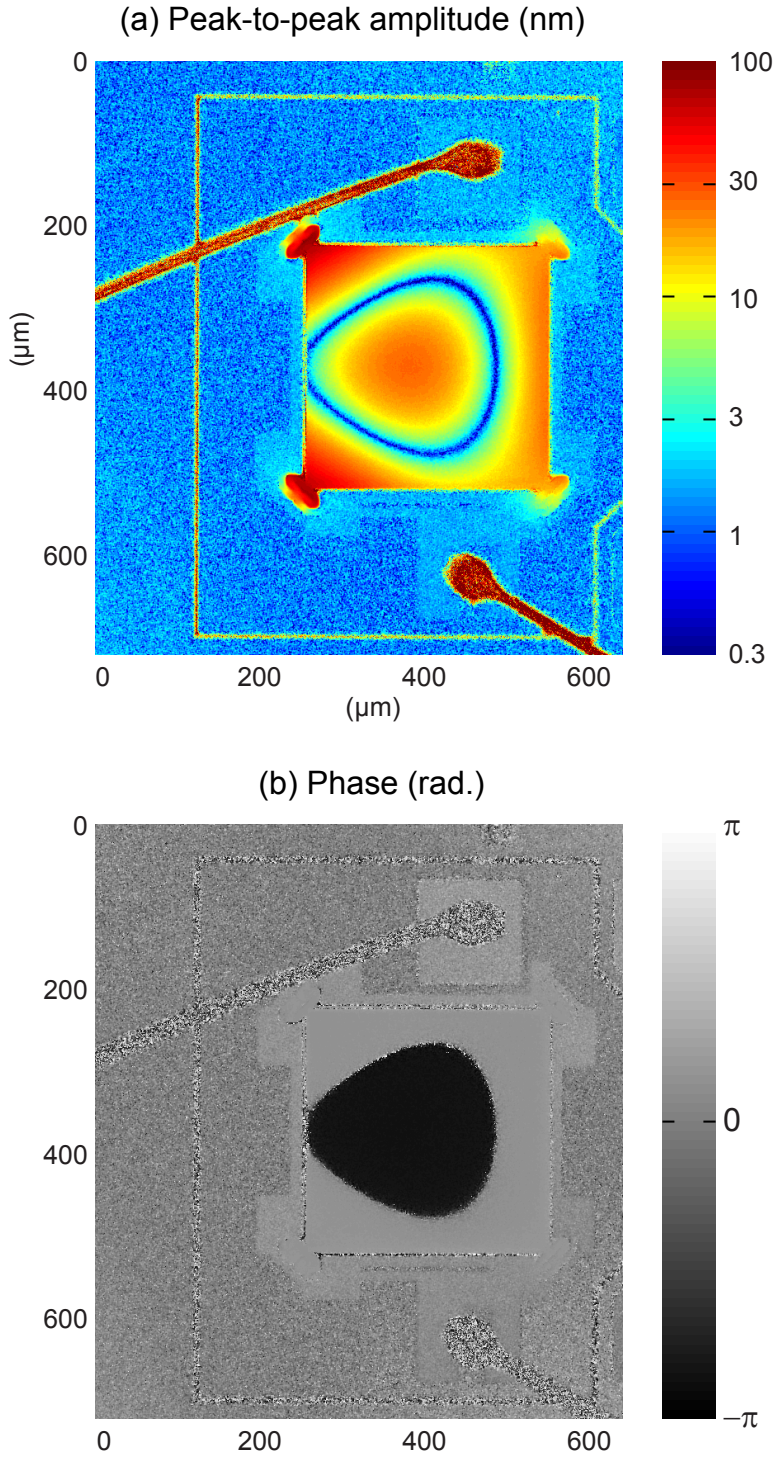

Figure 5.6. Measured vibration of the MEMS resonator sample, driven at 3.1926 MHz. **(a)** Amplitude of vibration, displayed in a logarithmic color scale. **(b)** Phase of vibration. In the resonance mode, the center and corners experiencing out-of-plane vibration at opposite phases. Around the center, an annular nodal line with zero amplitude can be observed. The phase measurement shows a clean phase change from $-\pi$ to 0 across the line. The dark thick bonding wires show no interference in the data and generate erroneus amplitude readings.

Chapter 6

Characterization

The performance of the measurement system depends on its many subsystems. The range of frequencies at which the surface vibrations can be probed is determined by the characteristics of the stroboscopic illumination system. The resolving power of the imaging optics combined with the pixel size of the sensor dictates the lateral resolution of the measurements. The vertical resolution of the obtained surface profiles is determined by the shape and signal to noise ratio of the measured data together with the choice of post processing methods. Finally, the ultimate characteristic of a measurement setup designed for studying surface vibration is defined by the limit of minimum detectable vibration amplitude.

As shown in the previous chapter, vibration on the order of a few megahertz is detectable with the current illumination system. Setting the light pulse length to as low as 40 ns is, however, at the performance limit of the system. The 33250A signal generator is capable of a minimum pulse length setting of 8 ns, but as suggested by figure 4.9, settings below 100 ns will not result in shorter pulses of the measured light output.

Being limited to light pulses in the order of 100 ns results in a duty cycle of 30% when measuring vibration at 3 MHz. When the light pulse is this long compared to the vibration period, significant motion blur will occur. However, even long duty cycles can reliably be used to detect sinusoidal vibration, provided that the pulse timing, i.e., the phase offset of the pulse can be controlled accurately. In these situations, the sinusoidal motion is convoluted by the long light pulse (motion blur) which results in a decreased amplitude measurement in the obtained sine curve data (figure 5.5(c)). [44]

While examining that figure, in which the sine curve traced by the surface position during one period of vibration is plotted, a systematic error in the measurement is evident. The comparison of measured points to the fitted sine curve shows that the values do not lie on the expected curve, most notably during the the beginning of the phase sweep. This effect regularly manifests itself in the same form and is most likely related to hysteresis in the z-translation mechanism. The problem is a likely

contributor in increasing the minimum detectable vibration amplitude and requires further work to be eliminated.

Pressure control during measurement is established by a vacuum system, which lowers the air pressure around the vibrating devices down to 0.1 mbar. At this pressure, the damping effect caused by air molecules are not a limiting factor in the performance of these resonators. [19]

In post processing of measured data, devices featuring structures of dielectric materials incur difficulties in accurately detecting the envelope peak location. In a measured surface profiles, surface position values can be considered consistent only in regions composed of the same material, because of different optical phase shifts on reflection off different materials.

Further difficulties in fringe locating are introduced by surfaces consisting of transparent thick layers, which reflect light from both top and bottom surfaces. They result an interferogram with two fringe patterns, with an example illustrated in figure 6.1. The distance between the the two patterns is related to the optical thickness of the film, i.e., the thickness physical thickness of the material multiplied by its refractive index, further multiplied by two to account the round-trip distance. [51] With a film thickness below the coherence length of the interferometer setup, the fringe patterns overlap and distort each other. Especially with structures of transparent material deposited on metal substrates, stronger reflection and therefore interference of stronger contrast is observed at the lower metal layer. This makes identifying and isolating the fringe pattern from the topmost reflection a difficult signal processing task.

Another problem is encountered during measurements of discrete steps with heights less than the coherence length of the interferometer. At the discontinuity, diffraction causes the contributions of the higher and lower surface to blend together and skew the fringe envelope, shifting its peak. This is a known physical effect known as *batwings*, referring to the shape of the anomalous features observed in the measured data. The problem is present in all well-established white light interferometer configurations. [52] The problem is illustrated in figure 6.2. Complex algorithms for removal of batwings have been proposed. [53] Batwings, however, are typically a bigger problem in absolute surface height profile measurements than in probing surface vibration of small amplitude on larger planar surfaces, like typical MEMS resonators.

The envelope location determination uses the phase information of the Hilbert transform to locate the exact zero phase point, which corresponds to the peak of a single fringe. However, with no further processing, it is not possible to guarantee that the correct fringe is obtained, if the rough location is first acquired from noisy envelope data. This leads to a problem of sporadic points with 2π ambiguity in the measurements. An error of 2π in phase corresponds to a surface height error of half a wavelength. Measurement data of a particularly pathological example is presented in figure 6.3. Unwrapping the discontinuities in two-dimensional data is difficult,

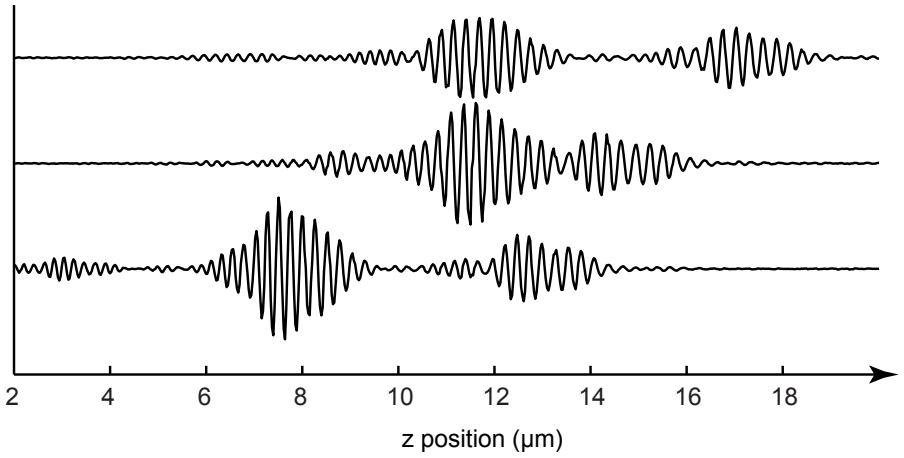

Figure 6.1. Examples of fringe patterns recorded of a BAW resonator device surface composed of transparent layers. The distance between two individual fringe envelopes is related to the layer thickness. With thin enough films, like with the middle interferogram pattern illustrated here, the fringe patterns overlap and distort each other, which then gives unreliable surface height values in post processing. Further difficulties are caused by the intensities of the top and bottom surface fringe patterns. The top surface fringes, in this image on the right hand side, are almost without exception weaker than the bottom reflection.

but the problem can be handled by processing of the interferogram phase data, as described in [53]. State-of-the-art post processing for white light interferogram data, carried out completely in the spatial frequency domain is described in [54].

The vertical resolution of surface profile measurements can be investigated by measurements of flat reference surfaces. However, acquiring a suitable reference flat surface is difficult. Reference flats are available down to a flatness of $\lambda/50$. This is in the order of 10 nanometers, which is much coarser than the vertical resolution of the white light interferometer. With measurement setups of sub-nanometer vertical resolution, the flatness requirements for reference surfaces approach the lattice constants of materials like silicon wafers and eventually, sizes of individual atoms. Furthermore, in an interferometric measurement, the acquired surface profile represents the difference between the sample and reference mirror surfaces, which adds difficulty in concluding what contributes to measured deviations.

Measurements were conducted with a flat silicon wafer. The tilt was adjusted such that the fringe oscillation happens as uniformly as possible over the entire one millimeter field of view of the camera. Typically, one is able to adjust tilt such that the entire field of view is covered by one fifth of a fringe width, by rough estimation. This might result from pinched optics or other wavefront distorting mechanism in the experimental setup, rather than actual differences between the surface profiles of the reference mirror and the silicon wafer.

The measured topography of the silicon wafer is illustrated in figure 6.4(a). The measurement is dominated by the wavefront mismatch, which is compensated by

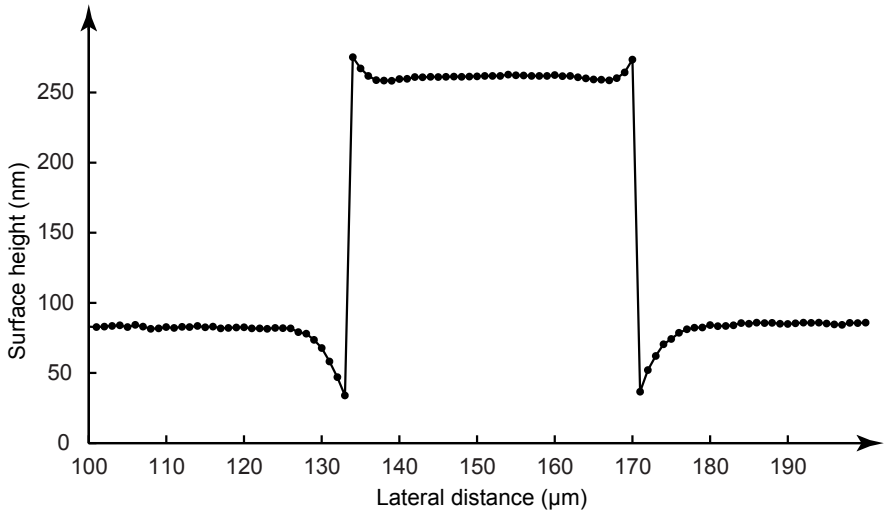

Figure 6.2. The measurement defect known as batwings. The cross section of a surface profile measured of a 180 nm step profile shows that the detected envelope is too high when close to the edge on the upper step and too low on the other side. The effect is caused by diffraction and is present in all white light interferometer systems.

subtracting a least squares fit of a two-dimensional polynomial surface, shown in (b). The difference (c) is then showing features of various size. They are not a result of imaging noise, which is visible at a finer resolution, but features of either the silicon wafer or reference mirror surfaces, or a combination of both.

Local standard deviation (STD) of measured values on the polynomial-corrected surface heavily depend on the size of the sampling area. Measurements of STD were done by randomly selecting 100 squares of equal size throughout the image and calculating the STD in each square and then calculating the average of those 100 STD's. The process was repeated for squares of different size to show the dependence of localization on STD. The estimated deviations are presented in figure 6.4(d).

Using a fairly large area of 150×150 pixels, the standard deviation of the surface profile is approximately 1 nm. However, a silicon wafer is unlikely to provide sub-nanometer flatness, which makes it possible that the actual measurement accuracy of the experimental setup is somewhere below the nanometer limit.

Mismatching wavefronts and uncertainties of reference mirror flatness are a problem for measurements of absolute surface profiles over wide lateral areas. In vibration measurements, however, reliable amplitude and phase readings can be obtained from relative surface position data, i.e., even if the position values would not be absolutely consistent over the whole field of view.

The most important characteristic of the interferometer system, the minimum detectable amplitude of vibration, can roughly be estimated from the vibration measurement data in figure 5.6. The noise floor of the measurement can be estimated by

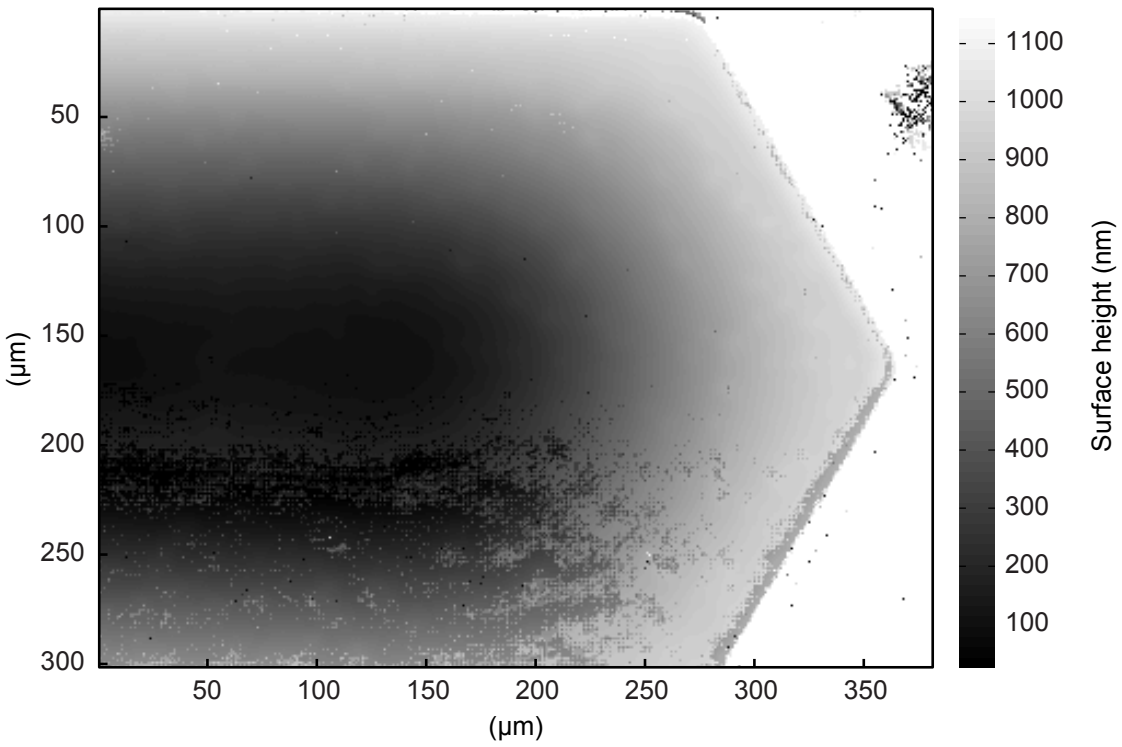

Figure 6.3. A height profile measurement of a deflected membrane. Most of the upper part of the membrane produces clean measurements, but the lower part is dominated by pixels with a false detection of -2π phase. This means that the pixels show the height value of the peak of one fringe below the correct one, which equals half the illumination wavelength or roughly 250 nm.

examining detected amplitude readings in stationary areas outside the resonating structure. These areas show amplitude values of approximately 1.3 ± 0.5 nm. Similar values are observed along the annular node of zero amplitude on the resonator plate.

The actual detection limit is difficult to determine based on a single measurement. A more thorough method of determining the lowest detectable amplitude would involve a series of measurements, attenuating the excitation power to the sample for bringing down the vibration amplitude. Judging from a single measurement, the lowest detectable amplitude of the current system is likely in the order of 1 nm. The system thus outperforms similar approaches [55] in the ability of acquiring reliable measurements of both higher frequencies and lower amplitudes.

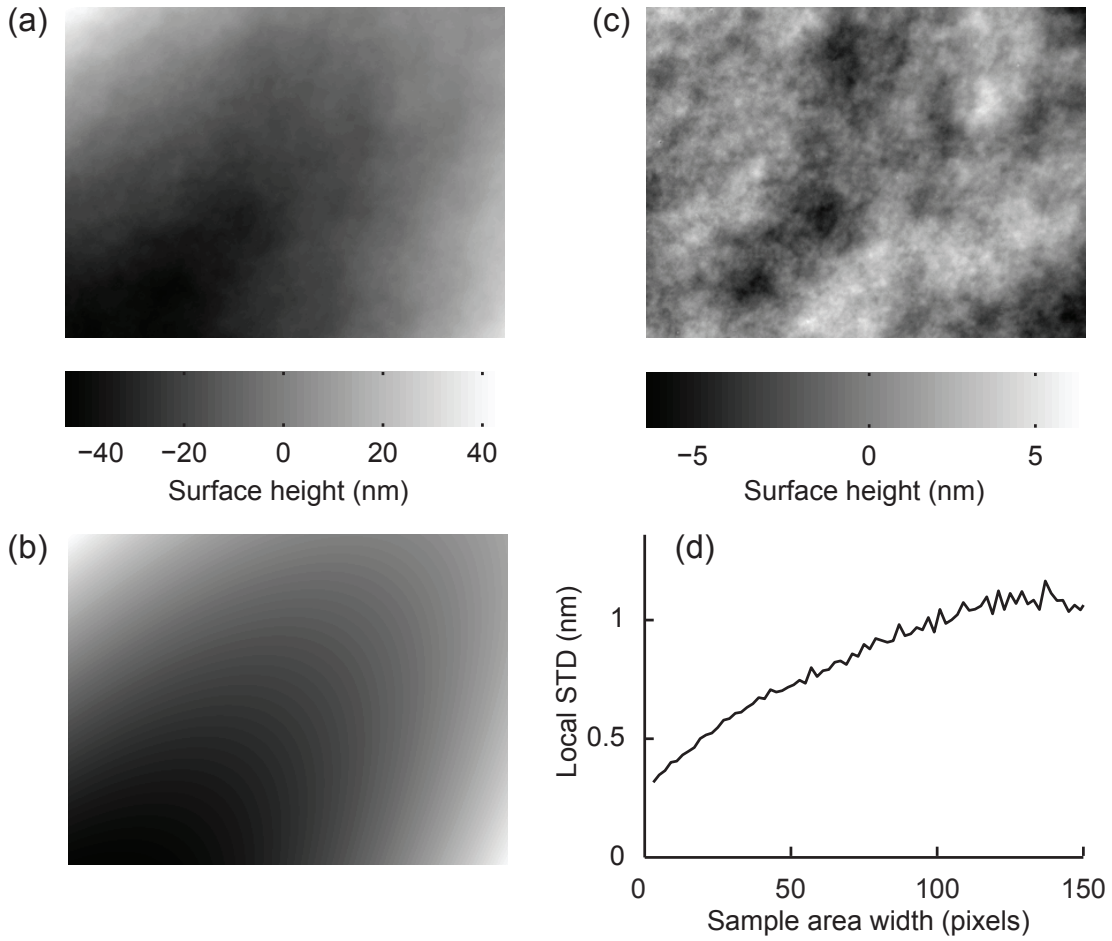

Figure 6.4. Determination of vertical resolution using a reference flat. The imaged area is 1280×960 pixels or roughly 1.3 × 1.0 mm of size. **(a)** Measured surface height map of a flat silicon wafer surface. The height extent is approximately 90 nm from peak to valley. The general curved profile is very likely to result from wavefront mismatch rather than actual surface profiles. **(b)** The profile is approximated with a two-dimensional second-degree polynomial surface, which is fitted with the least squares method and subtracted from the data. **(c)** After subtraction, the surface range is now around 10 nm and features of varying size are visible. **(d)** The local standard deviation (STD) was estimated as a function of sample area width.

Chapter 7

Conclusions

In this master's thesis, a stroboscopic white light interferometer microscope setup for the detection of minute surface vibration is designed, implemented and characterized. The implemented measurement system serves as a proof of concept for probing vibration in low-frequency electroacoustic devices with less hardware demand compared to, e.g., scanning laser interferometry. Direct optical measurements of surface vibration aid the research and development of these kind of devices, such as MEMS resonators.

The setup consists of a microscopic imaging system equipped with stroboscopic illumination for two-dimensional measurements of lateral vibration. Measurements are extended to the third dimension using optical interferometry. A Michelson interferometer is assembled between the microscope optics and the sample to acquire three-dimensional surface profiles of stationary targets. Periodic out-of-plane vibration of the surface is then measured utilizing stroboscopic illumination.

The capabilities of the system are demonstrated with measurements of out-of-plane vibration of a MEMS resonator device operating at 3 MHz. The lowest detectable amplitude is found to be approximately 1 nm.

Improving the current setup is feasible by refining the light pulsing system, the post processing algorithms and replacing the CCD camera. Currently, the shortest achievable light pulse duration is on the order of 100 ns. By redesigning the pulsing electronics, the duration could be expected to be brought down to around 10 ns, resulting in a ten-fold increase in the maximum measurement frequency. Using a monochrome camera without a color filter array would benefit both in lateral resolution and signal to noise ratio. By implementing state of the art post processing algorithms presented in literature, a sub-nanometer vertical resolution could be achieved.

References

[1] O. Holmgren. Laser-probe analysis of modern electroacoustic microwave devices. Ph.D. thesis. Helsinki University of Technology, 2009.

[2] J. Knuuttila, P. Tikka, and M. Salomaa. Scanning michelson interferometer for imaging surface acoustic wave fields. *Optics Letters* **25**:613–615, 2000.

[3] J. J. Yao. RF MEMS from a device perspective. *Journal of Micromechanics and Microengineering* **10**:R9, 2000.

[4] R. M. Finne and D. L. Klein. A water-amine-complexing agent system for etching silicon. **114**:965–970, 1967.

[5] O. N. Tufte, P. W. Chapman, and D. Long. Silicon Diffused-Element Piezoresistive Diaphragms. *Journal of Applied Physics* **33**:3322–3327, 1962.

[6] L. M. Roylance and J. B. Angell. A batch-fabricated silicon accelerometer. *IEEE Trans. Electron Devices* **26**:1911–1917, 1979.

[7] K. E. Petersen. Silicon as a mechanical material. *Proc. IEEE*, pp. 420–457. 1982. 70.

[8] Y. S. Hong, J. H. Lee, and S. H. Kim. A laterally driven symmetric microresonator for gyroscopic applications. *Journal of Micromechanics and Microengineering* **10**:452, 2000.

[9] Y. Ahn, H. Guckel, and J. D. Zook. Capacitive microbeam resonator design. *Journal of Micromechanics and Microengineering* **11**:70, 2001.

[10] A. Alastalo. Microelectromechanical resonator-based components for wireless communications: filters and transmission lines. Ph.D. thesis. VTT Technical Research Centre of Finland, 2006.

[11] G. Piazza. MEMS Resonators for Frequency Control and Sensing Applications. *IFCS/EFTF 2011, IEEE*, 2011.

[12] A. Witcrouw. CMOS-MEMS integration: Why, How and What? *Computer-Aided Design, ICCAD 2006, IEEE*, pp. 826 – 827. 2006.

[13] T. Mattila, J. Kiihamäki, T. Lamminmäki, O. Jaakkola, P. Rantakari, A. Oja, H. Seppä, H. Kattelus, and I. Tittonen. A 12 MHz micromechanical bulk acoustic mode oscillator. *Sensors and Actuators A: Physical* **101**:1 – 9, 2002.

[14] M. U. Demirci. Higher-mode free-free beam micromechanical resonators. *Proc. IEEE Int. Freq. Cont. Symp.*, pp. 810–818. 2003.

[15] V. Kaajakari, T. Mattila, A. Oja, J. Kiihamäki, and H. Seppä. Square-extensional mode single-crystal silicon micromechanical resonator for low phase noise oscillator applications. *Electron Dev. Lett.* , 2004.

[16] D. S. Bindel. Structured and parameter-dependent eigensolvers for simulation-based design of resonant MEMS. Ph.D. thesis. EECS Department, University of California, Berkeley, 2006.

[17] A. Bosseboeuf and S. Petitgrand. Characterization of the static and dynamic behaviour of m(o)ems by optical techniques: status and trends. *J. Micromech. Microeng.* **13**:S23–S33, 2003.

[18] R. M. A. Fatah. Electrostatic activation of micromechanical resonators. *Electron. Lett.* **27**:166–168, 1991.

[19] L. Kangas. Design and characterization of a vacuum system for interferometric measurements of MEMS resonators. Bachelor's thesis, Helsinki University of Technology (TKK), 2008.

[20] O. Holmgren, K. Kokkonen, T. Veijola, T. Mattila, V. Kaajakari, A. Oja, J. V. Knuuttila, and M. Kaivola. Analysis of vibration modes in a micromechanical square-plate resonator. *Journal of Micromechanics and Microengineering* **19**:015028, 2009.

[21] F. Yang, X. He, and C. Quan. Characterization of dynamic microgyroscopes by use of temporal digital image correlation. *Appl. Opt.* **45**:7785–7790, 2006.

[22] M. Guizar-Sicairos, S. Thurman, and J. Fienup. Efficient subpixel image registration algorithms. *Optics letters* **33**, 2008.

[23] W. Hemmert, M. S. Mermelstein, and D. M. Freeman. Nanometer resolution of three-dimensional motions using videointerference microscopy. *Proc. IEEE MEMS'99*, pp. 302–308. 1999.

[24] S. Donati. *Electro-Optical Instrumentation.* Prentice Hall, 2004.

[25] A. Michelson and E. Morley. On the relative motion of the earth and the luminiferous ether. *American Journal of Science* **34**:333–345, 1887.

[26] P. Hariharan. *Basics of Interferometry.* Academic Press, 1992.

[27] S. Malacara. *Optical Shop Testing.* John Wiley & Sons, 2007.

[28] P. de Groot and X. C. de Lega. Signal modeling for low-coherence height-scanning interference microscopy. *Appl. Opt.* **43**:4821–4830, 2004.

[29] I. Abdulhalim. Theory for double beam interference microscopes with coherence effects and verification using the linnik microscope. *Journal of Modern Optics* **48**:279–302, 2001.

[30] L. Kangas. Stroboscopic imaging of lateral vibrations in low-frequency MEMS resonators. Special assignment, Aalto University School of Science and Technology, 2010.

[31] A. Gock. Actual measured flash durations of small speedlight strobes. `http://www.gock.net/2012/01/flash-durations-small-strobes/`, 2012. [Online; accessed 2013-06-07].

[32] B. Serio, J. J. Hunsinger, D. D. Teyssieux, and B. Cretin. Phase correlation method for subpixel in-plane vibration measurements of MEMS by stroboscopic microscopy. *SPIE Conference series, vol. 5856*, pp. 755–762. 2005.

[33] Sony. ICX205AK - Diagonal 6mm (Type 1/3) Progressive Scan CCD Image Sensor with Square Pixel for Color Cameras. Datasheet.

[34] B. K. Gunturk, J. Glotzbach, Y. Altunbasak, R. W. Schafer, and R. M. Mersereau. Demosaicking: color filter array interpolation. *Signal Processing Magazine, IEEE* **22**:44–54, 2005.

[35] K. Hirakawa and T. W. Parks. Adaptive homogeneity-directed demosaicing algorithm. *Image Processing, IEEE Transactions on* **14**:360–369, 2005.

[36] B. E. Bayer. Color imaging array. , 1976. US Patent 3,971,065.

[37] L. A. J. Davis. Visualizing acoustic displacements of capacitive micromachined transducers using an interferometric microscope. *Acoustic Research Letters Online* **6**:75–79, 2005.

[38] O. Holmgren, K. Kokkonen, V. Kaajakari, A. Oja, and J. Knuuttila. Direct optical measurement of the Q values of RF-MEMS resonators. *Ultrasonics Symposium, 2005 IEEE*, 2005.

[39] D. Hils. Visual languages and computing survey: Data flow visual programming languages. *J. of Visual Languages & Computing* **3**:69–101, 1982.

[40] Agilent. *Agilent 33250A 80MHz Waveform Generator User's Guide*, 2003.

[41] R. Dändliker, E. Zimmermann, and G. Frosio. Electronically scanned white-light interferometry: a novel noise-resistant signal processing. *Opt. Lett.* **17**:679–681, 1992.

[42] S. Chen, A. W. Palmer, K. T. V. Grattan, and B. T. Meggitt. Digital signal-processing techniques for electronically scanned optical-fiber white-light interferometry. *Appl. Opt.* **31**:6003–6010, 1992.

[43] P. Pavliček and J. Soubusta. Measurement of the influence of dispersion on white-light interferometry. *Appl. Opt.* **43**:766–770, 2004.

[44] S. Petitgrand and A. Bosseboeuf. Simultaneous mapping of out-of-plane and in-plane vibrations of MEMS with (sub)nanometer resolution. *Journal of Micromechanics and Microengineering* **14**:S97, 2004.

[45] P. de Groot and L. Deck. Three-dimensional imaging by sub-nyquist sampling of white-light interferograms. *Opt. Lett.* **18**:1462–1464, 1993.

[46] K. G. Larkin. Efficient nonlinear algorithm for envelope detection in white light interferometry. *J. Opt. Soc. Am. A* **13**:832–843, 1996.

[47] S. S. C. Chim and G. S. Kino. Correlation microscope. *Opt. Lett.* **15**:579–581, 1990.

[48] E. Bedrosian. A product theorem for hilbert transforms. *Proceedings of the IEEE* **51**:868–869, 1963.

[49] P. de Groot and L. Deck. Surface profiling by analysis of white-light interferograms in the spatial frequency domain. *Journal of Modern Optics* **42**:389–401, 1995.

[50] A. Jaakkola, P. Rosenberg, S. Asmala, A. Nurmela, T. Pensala, T. Riekkinen, J. Dekker, T. Mattila, A. Alastalo, O. Holmgren *et al.*. Piezoelectrically transduced single-crystal-silicon plate resonators. *Ultrasonics Symposium, 2008. IUS 2008. IEEE*, pp. 717–720. IEEE, 2008.

[51] M. Conroy. Advances in thick and thin film analysis using interferometry. *Wear* **266**:502–506, 2009.

[52] A. Harasaki and J. C. Wyant. Fringe modulation skewing effect in white-light vertical scanning interferometry. *Appl. Opt.* **39**:2101–2106, 2000.

[53] A. Harasaki, J. Schmit, and J. C. Wyant. Improved vertical-scanning interferometry. *Appl. Opt.* **39**:2107–2115, 2000.

[54] P. de Groot, X. C. de Lega, J. Kramer, and M. Turzhitsky. Determination of fringe order in white-light interference microscopy. *Appl. Opt.* **41**:4571–4578, 2002.

[55] K. Hanhijärvi, I. Kassamakov, V. Heikkinen, J. Aaltonen, L. Sainiemi, K. Grigoras, S. Franssila, and E. Haeggstrom. Stroboscopic supercontinuum white-light interferometer for MEMS characterization. *Opt. Lett.* **37**:1703–1705, 2012.